Journal of Computational Physics 510 (2024) 113082

Contents lists available at ScienceDirect

Journal of Computational Physics

journal homepage: www.elsevier.com/locate/jcp

An efficient multi-field dynamic model for 3D wave propagation in saturated anisotropic porous media

Nico De Marchi [a], Giovanna Xotta [b,*], Massimiliano Ferronato [b], Valentina Salomoni [a]

[a] Department of Management and Engineering, University of Padova, Italy
[b] Department of Civil, Environmental and Architectural Engineering, University of Padova, Italy

ARTICLE INFO

Keywords:
Multi-field formulation
Porous media
Anisotropy
Iterative methods
Preconditioning

ABSTRACT

An efficient multi–field coupled dynamic model for saturated anisotropic porous materials is proposed here. The mathematical formulation of the dynamic deformation–diffusion problem is developed starting from the mixture theory and the definition of the effective stress for anisotropic poro–elasticity, taking into account also the fluid phase compressibility and anisotropic permeability. The effective stress principle is properly extended through the Biot tensor to predict the coupling between the shear stress of the solid skeleton and the pore fluid pressure. Numerical solution of the coupled problem is obtained by inf-sup stable Finite Element spaces. A fundamental issue for the computational efficiency of the coupled model is the numerical solution of the resulting large–size and non–symmetric discrete problem. In this work, we develop a fully implicit monolithic solver based on the Bi–Conjugate Gradient Stabilized (Bi-CGStab) algorithm accelerated via an ad–hoc Multi–Physics Reduction (MPR) preconditioning technique. The proposed advances are implemented in the 3D GeoMatFem research code and several numerical analyses are performed to test the potential and computational efficiency of the proposed tool. In particular, we focus on 3D wave propagation applications in fully saturated single and multi-layered anisotropic media. Numerical results show that our implementation is able to identify the shear wave splitting phenomenon due to the different degree of material symmetry between the solid phase and the whole porous material.

1. Introduction

Research and development of mathematical models describing the coupled multi–physical behavior of porous materials [1,2], along with their accurate, robust and efficient numerical implementation in modern computing machines, is still a compelling challenge for engineers and scientists in various fields, from structural mechanics, to geotechnics, reservoir engineering and biomechanics, e.g. [3–6]. Recent notable examples can be the influence of porosity content on the mechanical properties of composite laminates (carbon-fiber-reinforced plastics, CFRP) used in the design of aerospace or automotive components [7], or the inference of destructive seismic forces acting on buildings when appropriate seismic protection tools are in place [8], but also wave propagation through cancellous bones or tissues is an emerging application area to survey health status or any diseases [9].

Anisotropy of solid constituents is often a fundamental property to consider for an accurate representation of many materials at a macroscopic scale. Such solids exhibit a different mechanical response along some directions due to spatial inhomogeneity

* Corresponding author.
E-mail address: giovanna.xotta@unipd.it (G. Xotta).

https://doi.org/10.1016/j.jcp.2024.113082
Received 8 April 2023; Received in revised form 5 March 2024; Accepted 3 May 2024

Available online 9 May 2024
0021-9991/© 2024 The Authors. Published by Elsevier Inc. This is an open access article under the CC BY license (http://creativecommons.org/licenses/by/4.0/).

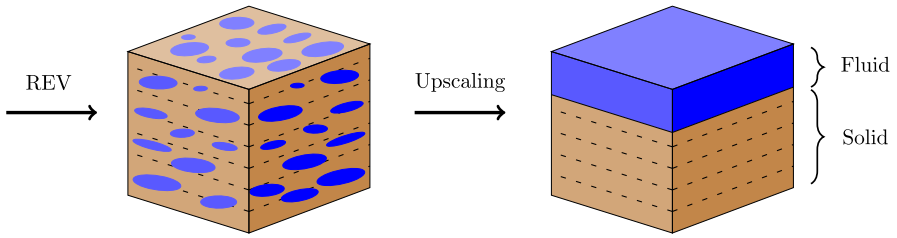

Fig. 1. REV for a fully saturated porous medium and its representation by Mixture Theory.

typically arising from the atomic arrangement (crystallography) or the micro– and macro–structure. Therefore, transverse isotropic, orthotropic, monoclinic and triclinic constitutive models [10] were developed, to properly describe for instance laminates, tissues, wood, some polymers, concrete, soils and rocks. In geophysics and geosciences, the detection of the degree of anisotropy through the study of wave propagation in geomaterials [11,12] can provide important pieces of information, not only on the mechanical properties of the solid, but also on the orientation and distribution of inner layers of water, gas, oil, coal and shale. In addition, in order to accurately represent the anisotropic medium it is also important to consider the different degree of anisotropy between the solid phase and the entire solid skeleton through the definition of an appropriate constitutive law linking stress and deformation of the porous medium with pore pressure [13]. In all these applications, the availability of a fully coupled multi-field model for the dynamic simulation of anisotropic porous materials is of paramount importance.

In the present work, we consider a two-phase (solid and fluid) material and follow the Mixture Theory [14] to establish the set of governing conservation laws. By using the generalized Hooke law with the definition of effective stress for anisotropic poro-elasticity [15,16] for the solid skeleton and the generalized Darcy law for the fluid part, the multi-field formulation of the governing dynamic PDEs in saturated porous materials is developed [17]. The numerical solution to the resulting initial-boundary value problem is obtained within the classical inf-sup stable Finite Element (FEM) framework in space [18–20] and the one–step generalized trapezoidal method (ϑ–Method) in time [21], while the non-linearities are addressed by a Newton procedure. The resulting discrete problem is solved in a fully implicit monolithic way, so as to preserve the coupling between the main variables also from a numerical point of view with no time step size restrictions with regard to the marching scheme stability [22]. However, fully implicit schemes require the solution to a time-sequence of large-size ill-conditioned block-structured linear systems. To this aim, the Bi-Conjugate Gradient Stabilized (Bi-CGStab, [23]) algorithm was used as a linear solver accelerated by an ad–hoc Multi–Physics Reduction (MPR) preconditioning technique [24–26] specifically developed for the coupled problem at hand. These advances are implemented in a *MATLAB* research code, called *GeoMatFEM* [27], used for coupled 3D dynamic geomechanical simulations. A set of numerical investigations, based on the work in Reference [28], are carried out to test the overall model efficiency and robustness. Finally, we consider the simulation of the shear wave splitting process in an anisotropic porous solid, providing evidence that the phenomenon can also occur as a result of a different degree of material symmetry axes between the solid phase and the whole medium.

The paper is organized as follows. First, the mathematical model describing the coupled dynamic deformation and fluid diffusion in saturated porous materials is reviewed and the numerical solution is described, with reference to the space and time integration strategies. Then, the original preconditioned iterative method for solving the time sequence of linear systems is presented and discussed in detail. In the numerical results section, three classes of dynamic analyses are presented: (i) the dynamic consolidation of a soil column, (ii) the propagation of plane waves in an anisotropic soil in plane strain conditions, and (iii) the simulation of the shear wave splitting phenomenon within a three dimensional fully saturated porous medium. The solver performance and robustness is discussed in detail with reference to the properties of the anisotropic constitutive model. Finally, a set of remarks close the presentation.

2. Governing equations

In this work, a two-phase porous material is considered, consisting of a solid matrix with relatively small interconnected pores that are completely filled by a fluid phase. Following the Mixture Theory [14], this saturated biphasic system can be represented by an effective medium in the Representative Elementary Volume (REV), where the distributions of the individual constituents are homogenized such that the volume of each material point within the REV is occupied by a fraction of solid and fluid constituents (Fig. 1).

The mass and linear momentum balance equations, governing this physical model in the dynamic regime for the two phases (index S for the solid-phase, F for the pore fluid phase), are defined as:

$$\rho^S \dot{\boldsymbol{v}} = \nabla \cdot \boldsymbol{\sigma}^S + \rho^S \boldsymbol{g} + \boldsymbol{h}^S \,, \tag{1a}$$

$$\rho^F \dot{\boldsymbol{w}} + \nabla \boldsymbol{w} \cdot \boldsymbol{w}_{\boldsymbol{R}} = \nabla \cdot \boldsymbol{\sigma}^F + \rho^F \boldsymbol{g} + \boldsymbol{h}^F \,, \tag{1b}$$

$$\dot{\rho^S} + \rho^S \nabla \cdot \boldsymbol{v} = 0 \,, \tag{1c}$$

$$\dot{\rho^F} + \rho^F \nabla \cdot \boldsymbol{w} = 0 \,, \tag{1d}$$

where $\rho^F = \varphi\rho_F$ and $\rho^S = (1-\varphi)\rho_S$ are the partial mass densities of the two phases, computed as the product of the volume fraction, with φ the porosity, and the intrinsic mass density, with $\sum_{\alpha=S,F}\rho^\alpha = \rho$; $\boldsymbol{v}, \boldsymbol{w}, \boldsymbol{w_R}$ are the solid, fluid and relative (fluid minus solid) velocity vectors; $\boldsymbol{\sigma}^\alpha$ is the partial Cauchy stress tensor of the α-phase; $\boldsymbol{g}$ is the gravitational acceleration and $\boldsymbol{h}^\alpha$ is the volume specific local interaction force between the phases, so that $\sum_{\alpha=S,F}\boldsymbol{h}^\alpha = \boldsymbol{0}$. Furthermore, we indicate by $(*)$ the material time derivative with respect to the motion of the solid phase, by $\nabla(*)$ the spatial gradient operator, by "$\cdot$" the scalar product and by $\nabla\cdot$ the divergence operator. Thermal effects as well as any mass exchange between the constituents are not taken into account here, while the compressibilities of the two phases are regarded with a standard barotropic state law.

Considering a homogeneous, linear elastic and anisotropic solid, the constitutive relationships for the solid matrix are provided by an extension of Terzaghi's principle, as illustrated in [13], and by Hooke's law:

$$\boldsymbol{\sigma'}^S = \boldsymbol{\sigma} + \boldsymbol{A}p = \mathbf{C} : \frac{1}{2}\left(\nabla\boldsymbol{u} + \nabla^T\boldsymbol{u}\right) = \mathbf{C} : \nabla^s\boldsymbol{u}, \tag{2a}$$

$$\boldsymbol{A} = \left(\mathbf{I} - \mathbf{C}\mathbf{S}_S\right) : \mathbf{1}, \tag{2b}$$

where $\boldsymbol{\sigma'}^S$ is the 2nd order effective stress tensor of the solid skeleton; $\boldsymbol{\sigma} = \boldsymbol{\sigma}^S + \boldsymbol{\sigma}^F$ is the total stress tensor of the mixture, sum of the partial stresses; $\boldsymbol{A}$ is the 2nd order Biot effective stress coefficient tensor; p is the pore fluid pressure; $\mathbf{C}$ is the 4th order elastic constitutive tensor of the mixture depending on the material proprieties; ∇^s denotes the symmetric gradient operator; $\boldsymbol{u}$ is the solid displacement vector, whereas $\mathbf{S}_S$ refers to the elastic compliance tensor of the solid part. As described in [15,16], the type of Biot tensor $\boldsymbol{A}$, namely full, diagonal or identity, depends on the degree of anisotropy of the solid phase and the entire porous material. In this work, the most general condition of a full Biot tensor is taken.

Generalized Darcy's law is considered as the constitutive equation for the fluid phase in laminar flow, relating the fluid flow rate to the pore pressure gradient:

$$\varphi\boldsymbol{w}_R = \left(-\boldsymbol{k}^F/\gamma_F\right)\nabla p, \tag{3}$$

where $\varphi\boldsymbol{w}_R$ is the Darcy velocity, $\boldsymbol{k}^F$ is the 2nd order hydraulic conductivity tensor, while $\gamma_F = \rho_F g$ is the fluid intrinsic unit weight, with $g = |\boldsymbol{g}|$ the scalar gravitational acceleration. The hydraulic conductivity tensor can be anisotropic and, if so, its components can be obtained through experimental methods [29]. Finally, for the volume-specific local interaction force $\boldsymbol{h}^F$ we have:

$$\boldsymbol{h}^F = -\varphi^2\gamma_F\boldsymbol{k}^{F,-1}\boldsymbol{w}_R + p\nabla\varphi \tag{4}$$

By combining the constitutive relationships (2) and (3) with the governing laws (1) and the force definition (4), the following set of partial differential equations (PDEs) is obtained:

$$\rho^S\dot{\boldsymbol{v}} = \nabla\cdot\left[\boldsymbol{\sigma'}^S - \left(\boldsymbol{A} - \varphi\mathbf{1}\right)p\right] + \rho^S\boldsymbol{g} + \varphi^2\gamma_F\boldsymbol{k}^{F,-1}\boldsymbol{w}_R - p\nabla\varphi, \tag{5a}$$

$$\rho^F\dot{\boldsymbol{w}} + \rho_F\nabla\boldsymbol{w}\cdot\boldsymbol{w}_R = -\varphi\nabla p + \rho^F\boldsymbol{g} - \varphi^2\gamma_F\boldsymbol{k}^{F,-1}\boldsymbol{w}_R, \tag{5b}$$

$$\Lambda\dot{p} + \boldsymbol{A} : \nabla^s\boldsymbol{v} + \frac{1}{\rho_F}\nabla\cdot\left(\rho^F\boldsymbol{w}_R\right) = 0, \tag{5c}$$

where the first and the second equations prescribe the momentum balance of the solid and fluid phases, respectively, while the third one is the mass balance of the entire mixture obtained by considering the same procedure described in [30] properly extended to an anisotropic medium. The scalar quantity Λ is the compressibility modulus, computed as [15]:

$$\Lambda = \frac{(1-\varphi)}{\mathsf{K}_S} + \frac{\varphi}{\mathsf{K}_F} - \boldsymbol{A} : \mathbf{S} : \boldsymbol{A} = \frac{(1-\varphi)}{\mathsf{K}_S} + \frac{\varphi}{\mathsf{K}_F} - \mathbf{1} : \mathbf{S}_S\mathbf{C}\mathbf{S}_S : \mathbf{1}, \tag{6}$$

with K_α the bulk modulus of the α-phase and $\mathbf{S}$ the elastic compliance tensor of the entire mixture. By considering the small strain hypothesis, the coupled equations (5a)-(5c) are linear and, in addition, by assuming that $\varphi \approx \varphi_0$, $\nabla\varphi \approx \boldsymbol{0}$, the convective term $\nabla\boldsymbol{w}\cdot\boldsymbol{w}_R \approx \boldsymbol{0}$ and the fluid density gradient $\nabla\rho^F \approx \boldsymbol{0}$ can be overlooked.

To simultaneously compute the solid displacement and velocity, the corresponding strong definition, i.e., $\dot{\boldsymbol{u}} = \boldsymbol{v}$, is added to the previous set of governing PDEs. Finally, in order to improve the stability of the numerical solution [17], equations are rearranged by adding the linear momentum of fluid phase (5b) to the linear momentum of solid phase (5a) and to the mass balance equation (5c), so as to obtain the governing initial-boundary value problem (IBVP) that follows.

Let $\Omega \subset \mathbb{R}^d$ and Γ denote the domain occupied by a porous medium and its boundary, respectively, with $\boldsymbol{x}$ the position vector in $\mathbb{R}^d$ and $d = 2,3$ the problem dimension. We indicate the time with t, belonging to an open interval $\mathcal{I} =]0,T[$ of length $T > 0$, while a bar above a set in $\mathbb{R}^d$ denotes the union of the same set with its boundary, e.g. $\overline{\Omega} = \Omega \cup \Gamma$. The boundary is decomposed as $\Gamma = \overline{\Gamma_u \cup \Gamma_\sigma} = \overline{\Gamma_p \cup \Gamma_q}$, with $\Gamma_u \cap \Gamma_\sigma = \Gamma_p \cap \Gamma_q = \emptyset$, and $\boldsymbol{n}$ denotes its outer normal vector. Then, we want to find the functions: $\boldsymbol{u} : \overline{\Omega}\times[0,T] \to \mathbb{R}^d$ (displacement), $\boldsymbol{v} : \overline{\Omega}\times[0,T] \to \mathbb{R}^d$ (solid velocity), $\boldsymbol{w} : \overline{\Omega}\times[0,T] \to \mathbb{R}^d$ (fluid velocity), $p : \overline{\Omega}\times[0,T] \to \mathbb{R}$ (pressure), such that:

$$\dot{\boldsymbol{u}} - \boldsymbol{v} = \boldsymbol{0}, \qquad \text{in } \Omega\times\mathcal{I}, \tag{7a}$$

$$(1-\varphi)\rho_S\dot{\boldsymbol{v}} + \varphi\rho_F\dot{\boldsymbol{w}} - \nabla\cdot(\mathbf{C} : \nabla^s\boldsymbol{u} - \boldsymbol{A}p) = \rho\boldsymbol{g}, \qquad \text{in } \Omega\times\mathcal{I}, \tag{7b}$$

$$\rho_F\dot{\boldsymbol{w}} - \varphi\gamma_F\boldsymbol{k}^{F,-1}\boldsymbol{v} + \varphi\gamma_F\boldsymbol{k}^{F,-1}\boldsymbol{w} + \nabla p = \rho_F\boldsymbol{g}, \qquad \text{in } \Omega\times\mathcal{I}, \tag{7c}$$

$$-\nabla\cdot\left(\frac{\boldsymbol{k}^F}{g}\dot{\boldsymbol{w}}\right)+\Lambda\dot{p}+\boldsymbol{A}:\nabla^s\dot{\boldsymbol{v}}-\nabla\cdot\left(\frac{\boldsymbol{k}^F}{\gamma_F}\nabla p\right)=-\nabla\cdot\left(\frac{\boldsymbol{k}^F}{g}\boldsymbol{g}\right),\qquad\text{in }\Omega\times\mathcal{I},\tag{7d}$$

with the following set of boundary and initial conditions:

$$\boldsymbol{u}=\bar{\boldsymbol{u}},\qquad\text{on }\Gamma_u\times\mathcal{I},\tag{8a}$$

$$(\mathbf{C}:\nabla^s\boldsymbol{u}-\boldsymbol{A}p)\cdot\boldsymbol{n}=\bar{\boldsymbol{t}},\qquad\text{on }\Gamma_\sigma\times\mathcal{I},\tag{8b}$$

$$\left(\frac{\boldsymbol{k}^F}{\gamma_F}\nabla p\right)\cdot\boldsymbol{n}=\bar{q},\qquad\text{on }\Gamma_q\times\mathcal{I},\tag{8c}$$

$$p=\bar{p},\qquad\text{on }\Gamma_p\times\mathcal{I},\tag{8d}$$

$$\boldsymbol{u}(\boldsymbol{x},0)=\boldsymbol{u}_0,\qquad\boldsymbol{x}\in\overline{\Omega},\tag{8e}$$

$$\boldsymbol{v}(\boldsymbol{x},0)=\boldsymbol{v}_0,\qquad\boldsymbol{x}\in\overline{\Omega},\tag{8f}$$

$$p(\boldsymbol{x},0)=p_0,\qquad\boldsymbol{x}\in\overline{\Omega},\tag{8g}$$

where $\bar{\boldsymbol{u}}$, $\bar{\boldsymbol{t}}$, $\bar{q}$, and $\bar{p}$ are the prescribed boundary displacement, traction, fluid flux and excess pore pressure, respectively, whereas $\boldsymbol{u}_0$, $\boldsymbol{v}_0$, and p_0 are the initial displacement, solid velocity and excess pore pressure. The solid velocity definition and generalized Darcy's law along the domain boundary and at the initial instant close the formulation:

$$\boldsymbol{v}=\dot{\boldsymbol{u}},\qquad\text{on }\Gamma\times\mathcal{I},\tag{9a}$$

$$\boldsymbol{w}=-\frac{\boldsymbol{k}^F}{\varphi\gamma_F}\nabla p+\boldsymbol{v},\qquad\text{on }\Gamma\times\mathcal{I},\tag{9b}$$

$$\boldsymbol{w}(\boldsymbol{x},0)=-\frac{\boldsymbol{k}^F}{\varphi\gamma_F}\nabla p_0+\boldsymbol{v}_0,\qquad\boldsymbol{x}\in\overline{\Omega}.\tag{9c}$$

Following the usual notation, let us denote by $H^1(\Omega)$ and $\boldsymbol{H}^1(\Omega)$ the Sobolev space of scalar and vector functions, respectively, whose first derivatives are square-integrable, i.e., they belong to the Lebesgue space $L^2(\Omega)$; by $\boldsymbol{H}(\mathrm{div};\Omega)$ the Sobolev space of vector functions with square-integrable divergence; by $H^1_0(\Omega)$, $\boldsymbol{H}^1_0(\Omega)$ and $\boldsymbol{H}_0(\mathrm{div};\Omega)$ the corresponding spaces with null trace on Γ, and by $\boldsymbol{H}^{1/2}(\Gamma)$ the space of square-integrable traces on Γ of vector functions in $\boldsymbol{H}^1(\Omega)$. Introducing the spaces:

$$\mathcal{U}=\{\boldsymbol{u}\in\boldsymbol{H}^1(\Omega)\ \mid\ \boldsymbol{u}|_{\Gamma_u}=\bar{\boldsymbol{u}}\in\boldsymbol{H}^{1/2}(\Gamma)\},\tag{10a}$$

$$\mathcal{V}=\{\boldsymbol{v}\in\boldsymbol{H}^1(\Omega)\ \mid\ \boldsymbol{v}|_{\Gamma}=\dot{\boldsymbol{u}}\in\boldsymbol{H}^{1/2}(\Gamma)\},\tag{10b}$$

$$\mathcal{W}=\{\boldsymbol{w}\in\boldsymbol{H}(\mathrm{div};\Omega)\ \mid\ \boldsymbol{w}|_{\Gamma}=-\frac{\boldsymbol{k}^F}{\varphi\gamma_F}\nabla p+\boldsymbol{v}\},\tag{10c}$$

$$\mathcal{P}=\{p\in H^1_0(\Omega)\},\tag{10d}$$

the weak form of the IBVP (7) reads: for every time $t\in\mathcal{I}$ find $\{\boldsymbol{u},\boldsymbol{v},\boldsymbol{w},p\}\in\mathcal{U}\times\mathcal{V}\times\mathcal{W}\times\mathcal{P}$ such that:

$$a(\boldsymbol{\psi},\boldsymbol{u},\boldsymbol{v})=0,\qquad\forall\boldsymbol{\psi}\in\boldsymbol{H}^1_0(\Omega),\tag{11a}$$

$$b(\boldsymbol{\psi},\boldsymbol{u},\boldsymbol{v},\boldsymbol{w},p)=(\boldsymbol{\psi},\rho\boldsymbol{g})_\Omega+(\boldsymbol{\psi},\bar{\boldsymbol{t}})_{\Gamma_\sigma},\qquad\forall\boldsymbol{\psi}\in\boldsymbol{H}^1_0(\Omega),\tag{11b}$$

$$c(\boldsymbol{\phi},\boldsymbol{v},\boldsymbol{w},p)=(\boldsymbol{\phi},\rho_F\boldsymbol{g})_\Omega-(\boldsymbol{\phi}\cdot\boldsymbol{n},\bar{p})_{\Gamma_p},\qquad\forall\boldsymbol{\phi}\in\boldsymbol{\mathcal{H}}_0(\mathrm{div},\Omega),\tag{11c}$$

$$d(\eta,\boldsymbol{v},\boldsymbol{w},p)=(\eta,\mathrm{div}\,\frac{\boldsymbol{k}^F}{g}\boldsymbol{g})_\Omega+(\eta,\bar{q})_{\Gamma_q},\qquad\forall\eta\in H^1_0(\Omega),\tag{11d}$$

where $a(\cdot)$, $b(\cdot)$, $c(\cdot)$, and $d(\cdot)$ are the bilinear forms:

$$a(\boldsymbol{\psi},\boldsymbol{u},\boldsymbol{v})=(\boldsymbol{\psi},\dot{\boldsymbol{u}})_\Omega-(\boldsymbol{\psi},\boldsymbol{v})_\Omega,\tag{12a}$$

$$b(\boldsymbol{\psi},\boldsymbol{u},\boldsymbol{v},\boldsymbol{w},p)=(\boldsymbol{\psi},\rho^S\dot{\boldsymbol{v}})_\Omega+(\boldsymbol{\psi},\rho^F\dot{\boldsymbol{w}})_\Omega+(\nabla^s\boldsymbol{\psi},\mathbf{C}:\nabla^s\boldsymbol{u})_\Omega-(\nabla^s\boldsymbol{\psi},\boldsymbol{A}p)_\Omega,\tag{12b}$$

$$c(\boldsymbol{\phi},\boldsymbol{v},\boldsymbol{w},p)=(\boldsymbol{\phi},\rho_F\dot{\boldsymbol{w}})_\Omega-(\boldsymbol{\phi},\varphi\gamma_F\boldsymbol{k}^{F,-1}\boldsymbol{v})_\Omega+(\boldsymbol{\phi},\varphi\gamma_F\boldsymbol{k}^{F,-1}\boldsymbol{w})_\Omega-(\mathrm{div}\,\boldsymbol{\phi},p)_\Omega,\tag{12c}$$

$$d(\eta,\boldsymbol{v},\boldsymbol{w},p)=(\eta,\mathrm{div}\,\frac{\boldsymbol{k}^F}{\gamma_F}\dot{\boldsymbol{w}})_\Omega+(\eta,\Lambda\dot{p})_\Omega+(\eta,\boldsymbol{A}:\nabla^s\boldsymbol{v})_\Omega+(\nabla\eta,\frac{\boldsymbol{k}^F}{\gamma_F}\nabla p)_\Omega,\tag{12d}$$

and $(\cdot,\cdot)_\Omega$ denote the inner products of scalar functions in $L^2(\Omega)$, vector functions in $[L^2(\Omega)]^d$, or second-order tensor functions in $[L^2(\Omega)]^{d\times d}$, as appropriate, and $(\cdot,\cdot)_{\Gamma_*}$ denote the inner products of scalar functions or vector functions on the boundary Γ_*.

3. Numerical model

3.1. Space and time discretization

By approximating the weak form (11) via a Finite Element approach and replacing the continuous with the corresponding discrete spaces, the following system of 1st order differential equations in time is obtained:

$$\mathbf{M}\dot{\mathbf{z}} + \mathbf{K}\mathbf{z} + \mathbf{f} = \mathbf{0}, \tag{13}$$

where:

- $\mathbf{z} = [\mathbf{u}; \mathbf{v}; \mathbf{w}; \mathbf{p}]^T$ is the vector of discrete $n_u + n_v + n_w + n_p$ unknowns;
- $\mathbf{M}$ and $\mathbf{K}$ are the global mass and stiffness matrix, respectively:

$$\mathbf{M} = \begin{bmatrix} I_u & 0 & 0 & 0 \\ 0 & M_{vv} & M_{vw} & 0 \\ 0 & 0 & M_{ww} & 0 \\ 0 & 0 & M_{pw} & M_{pp} \end{bmatrix}, \quad \mathbf{K} = \begin{bmatrix} 0 & -I_u & 0 & 0 \\ K_{vu} & 0 & 0 & K_{vp} \\ 0 & K_{wv} & K_{ww} & K_{wp} \\ 0 & K_{pv} & 0 & K_{pp} \end{bmatrix}, \tag{14}$$

- $\mathbf{f} = [\mathbf{0}; \mathbf{f}_v; \mathbf{f}_w; \mathbf{f}_p]^T$ is the vector collecting the forcing functions and natural boundary conditions for the solid velocity ($\mathbf{f}_v$), fluid velocity ($\mathbf{f}_w$), and pressure ($\mathbf{f}_p$).

Full details on the specific form of every block of equations (14) are reported in Appendix A.

The differential-algebraic system (13) is solved in time by the standard ϑ-Method, which leads to the following recurring expression of the residual:

$$\bar{\mathbf{b}} = \left[\vartheta \mathbf{K}_{t^*} + \frac{\mathbf{M}_{t^*}}{\Delta t_n}\right]\mathbf{z}_{n+1} - \left[\frac{\mathbf{M}_{t^*}}{\Delta t_n} - (1-\vartheta)\,\mathbf{K}_{t^*}\right]\mathbf{z}_n + \vartheta \mathbf{f}_{n+1} + (1-\vartheta)\,\mathbf{f}_n = 0, \tag{15}$$

with time $t^* = \vartheta t_{n+1} + (1-\vartheta)\,t_n$, $\vartheta \in [0,1]$. Equation (15) is weakly non-linear because of the compressibility of the phases, hence a Newton scheme is implemented. We require the norm of the residual $\bar{\mathbf{b}}$ to be smaller than a prescribed tolerance, otherwise a correction of the solution vector $\mathbf{z}_{n+1}$ is necessary. This update is computed at Newton step $i+1$ by adding the increment $d\mathbf{z} = [d\mathbf{u}; d\mathbf{v}; d\mathbf{w}; d\mathbf{p}]^T$ to the previously computed solution vector $\mathbf{z}^i_{n+1}$ through the following linear system with size $n_u + n_v + n_w + n_p$:

$$\bar{\mathbf{A}}\, d\mathbf{z} = \bar{\mathbf{b}}^i, \tag{16}$$

where $\bar{\mathbf{b}}^i$ is the residual (15) computed in $\mathbf{z}^i_{n+1}$. The system matrix $\bar{\mathbf{A}}$ has the following form:

$$\bar{\mathbf{A}} = \begin{bmatrix} I_u/\Delta t_n & -\vartheta I_u & 0 & 0 \\ \vartheta K_{vu} & M_{vv}/\Delta t_n & M_{vw}/\Delta t_n & \vartheta K_{vp} \\ 0 & \vartheta K_{wv} & \vartheta K_{ww} + M_{ww}/\Delta t_n & \vartheta K_{wp} \\ 0 & \vartheta K_{pv} & M_{pw}/\Delta t_n & \vartheta K_{pp} + M_{pp}/\Delta t_n \end{bmatrix}, \tag{17}$$

where the time increment index in the matrix has been removed for better reading.

By explicitly writing the first equation in (16), we can derive the displacement increment $d\mathbf{u}$:

$$d\mathbf{u} = \vartheta \Delta t_n\, d\mathbf{v} + \mathbf{u}^i_{n+1} - \vartheta \Delta t_n \mathbf{v}^i_{n+1} - \mathbf{u}_n - (1-\vartheta)\,\Delta t_n \mathbf{v}_n, \tag{18}$$

which, substituted into the second equation, allows us to reduce the dimension of the system. This gives the reduced form for the residual $\mathbf{b} = [\mathbf{b}_v; \mathbf{b}_w; \mathbf{b}_p]^T$:

$$\begin{aligned} \mathbf{b}_v =& [M_{vv}/\Delta t_n + \vartheta^2 \Delta t_n K_{vu}]\mathbf{v}^i_{n+1} + M_{vw}/\Delta t_n \mathbf{w}^i_{n+1} + \vartheta K_{vp}\mathbf{p}^i_{n+1} \\ &+ K_{vu}\mathbf{u}_n - [M_{vv}/\Delta t_n - \vartheta(1-\vartheta)\Delta t_n K_{vu}]\mathbf{v}_n - M_{vw}/\Delta t_n \mathbf{w}_n + (1-\vartheta)K_{vp}\mathbf{p}_n \\ &+ \vartheta \mathbf{f}^{(v)}_{n+1} + (1-\vartheta)\mathbf{f}^{(v)}_n, \end{aligned} \tag{19}$$

$$\begin{aligned} \mathbf{b}_w =& \vartheta K_{wv}\mathbf{v}^i_{n+1} + [M_{ww}/\Delta t_n + \vartheta K_{ww}]\mathbf{w}^i_{n+1} + \vartheta K_{wp}\mathbf{p}^i_{n+1} \\ &+ (1-\vartheta)K_{wv}\mathbf{v}_n - [M_{ww}/\Delta t_n - (1-\vartheta)K_{ww}]\mathbf{w}_n + (1-\vartheta)K_{wp}\mathbf{p}_n \\ &+ \vartheta \mathbf{f}^{(w)}_{n+1} + (1-\vartheta)\mathbf{f}^{(w)}_n, \end{aligned} \tag{20}$$

$$\begin{aligned} \mathbf{b}_w =& \vartheta K_{pv}\mathbf{v}^i_{n+1} + M_{pw}/\Delta t_n \mathbf{w}^i_{n+1} + [M_{pp}/\Delta t_n + \vartheta K_{pp}]\mathbf{p}^i_{n+1} \\ &+ (1-\vartheta)K_{pv}\mathbf{v}_n - M_{pw}/\Delta t_n \mathbf{w}_n - [M_{pp}/\Delta t_n - (1-\vartheta)K_{pp}]\mathbf{p}_n \end{aligned}$$

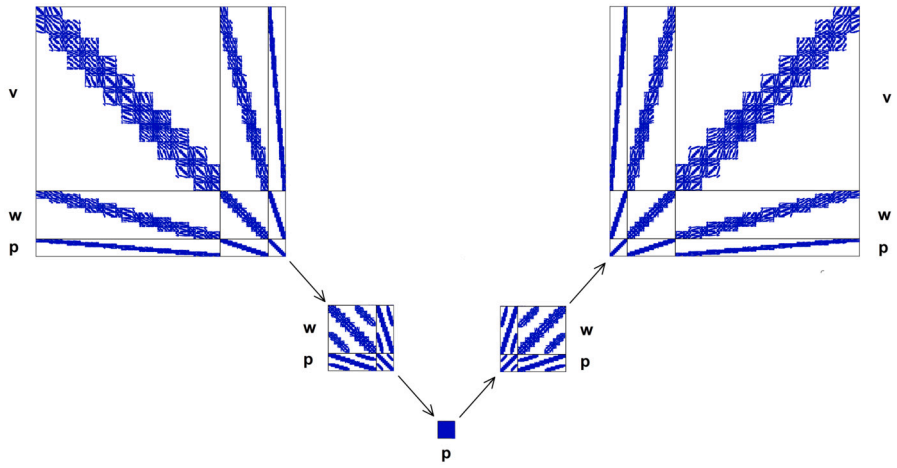

Fig. 2. Sketch of the MPR approach.

$$+ \vartheta \mathbf{f}_{n+1}^{(p)} + (1-\vartheta)\mathbf{f}_n^{(p)}, \tag{21}$$

and the system matrix $\mathbf{A}$:

$$\mathbf{A} = \begin{bmatrix} \vartheta^2 \Delta t_n K_{vu} + \frac{M_{vv}}{\Delta t_n} & \frac{M_{vw}}{\Delta t_n} & \vartheta K_{vp} \\ \vartheta K_{wv} & \vartheta K_{ww} + \frac{M_{ww}}{\Delta t_n} & \vartheta K_{wp} \\ \vartheta K_{pv} & \frac{M_{pw}}{\Delta t_n} & \vartheta K_{pp} + \frac{M_{pp}}{\Delta t_n} \end{bmatrix} = \begin{bmatrix} A_{vv} & A_{vw} & A_{vp} \\ A_{wv} & A_{ww} & A_{wp} \\ A_{pv} & A_{pw} & A_{pp} \end{bmatrix}. \tag{22}$$

A key issue for the application of the proposed 3-field dynamic poro-elastic model in real-world problems is the efficient solution, at every Newton iteration in every time step, of the block linear system:

$$\mathbf{A}\mathbf{x} = \mathbf{b}, \tag{23}$$

where $\mathbf{A}$ is the system matrix (22), $\mathbf{b}$ is the residual vector (19) – (21), and $\mathbf{x} = [d\mathbf{v}; d\mathbf{w}; d\mathbf{p}]^T$ is the increment of the solution.

3.2. Linear solver

It is easy to observe that the diagonal blocks of $\mathbf{A}$, i.e., A_{vv}, A_{ww} and A_{pp}, are Symmetric Positive Definite (SPD) matrices. However, generally $A_{vw} \neq A_{wv}^T$, $A_{vp} \neq A_{pv}^T$, and $A_{wp} \neq A_{pw}^T$, so the overall system is non-symmetric. Therefore, Krylov methods such as the Generalized Minimal Residual (GMRES, [31]) or the Bi-Conjugate Gradient Stabilized (Bi-CGStab, [23]) should be used for large-size problems.

It is very well-known that the use of a preconditioner, $\mathbf{P}^{-1}$, is necessary to accelerate the convergence of the linear solver [32–34]. Generally speaking, we denote as preconditioner $\mathbf{P}^{-1}$ of $\mathbf{A}$ a non-singular operator whose application to a vector resembles as much as possible that of $\mathbf{A}^{-1}$. It is not necessary to know $\mathbf{P}^{-1}$ explicitly, the only algorithm needed being the sequence of operations required to compute $\mathbf{g} \in \mathbb{R}^{n_v+n_w+n_p}$ equal to $\mathbf{P}^{-1}\mathbf{r}$ for some given vector $\mathbf{r} \in \mathbb{R}^{n_v+n_w+n_p}$. Here we use a Multi-Physics Reduction (MPR) approach that progressively restricts the system to a single-physics problem and then prolongs it back to the fully-coupled problem (Fig. 2). Of course, each restriction fills the reduced matrix, so that it must be carried out approximately. According to the selected sequence of reductions, different algorithms may arise. In this work, we follow the natural sequence going from the largest to the smallest physical block, i.e., solid velocity–fluid velocity–pressure. The proposed MPR approach can be also recast in other similar frameworks, such as the MultiGrid Reduction [35,36] or the general algebraic method proposed in the context of coupled contact and poro-mechanics [25,37].

Let us partition $\mathbf{r}$ and $\mathbf{g}$ as $\mathbf{r} = [\mathbf{r}_v; \mathbf{r}_w; \mathbf{r}_p]^T$ and $\mathbf{g} = [\mathbf{g}_v; \mathbf{g}_w; \mathbf{g}_p]^T$, with $\mathbf{r}_v, \mathbf{g}_v \in \mathbb{R}^{n_v}$, $\mathbf{r}_w, \mathbf{g}_w \in \mathbb{R}^{n_w}$, and $\mathbf{r}_p, \mathbf{g}_p \in \mathbb{R}^{n_p}$. The exact application of $\mathbf{A}^{-1}$ to $\mathbf{r}$ would require the solution of the system:

$$\begin{cases} A_{vv}\mathbf{g}_v + A_{vw}\mathbf{g}_w + A_{vp}\mathbf{g}_p &= \mathbf{r}_v \\ A_{wv}\mathbf{g}_v + A_{ww}\mathbf{g}_w + A_{wp}\mathbf{g}_p &= \mathbf{r}_w \\ A_{pv}\mathbf{g}_v + A_{pw}\mathbf{g}_w + A_{pp}\mathbf{g}_p &= \mathbf{r}_p \end{cases}. \tag{24}$$

Compute $\mathbf{g}_v$ from the first equation:

$$\mathbf{g}_v = A_{vv}^{-1}\left(\mathbf{r}_v - A_{vw}\mathbf{g}_w - A_{vp}\mathbf{g}_p\right), \tag{25}$$

and introduce equation (25) in the second and third equation of (24), thus eliminating $\mathbf{g}_v$:

$$\begin{cases} \left(A_{ww} - A_{wv}A_{vv}^{-1}A_{vw}\right)\mathbf{g}_w + \left(A_{wp} - A_{wv}A_{vv}^{-1}A_{vp}\right)\mathbf{g}_p &= \mathbf{r}_w - A_{wv}A_{vv}^{-1}\mathbf{r}_v \\ \left(A_{pw} - A_{pv}A_{vv}^{-1}A_{vw}\right)\mathbf{g}_w + \left(A_{pp} - A_{pv}A_{vv}^{-1}A_{vp}\right)\mathbf{g}_p &= \mathbf{r}_p - A_{pv}A_{vv}^{-1}\mathbf{r}_v \end{cases} . \tag{26}$$

Setting:

$$B_{ww} = A_{ww} - A_{wv}A_{vv}^{-1}A_{vw}, \tag{27a}$$

$$B_{wp} = A_{wp} - A_{wv}A_{vv}^{-1}A_{vp}, \tag{27b}$$

$$B_{pw} = A_{pw} - A_{pv}A_{vv}^{-1}A_{vw}, \tag{27c}$$

$$B_{pp} = A_{pp} - A_{pv}A_{vv}^{-1}A_{vp}, \tag{27d}$$

the reduced system (26) reads:

$$\begin{cases} B_{ww}\mathbf{g}_w + B_{wp}\mathbf{g}_p &= \mathbf{r}_w - A_{wv}A_{vv}^{-1}\mathbf{r}_v \\ B_{pw}\mathbf{g}_w + B_{pp}\mathbf{g}_p &= \mathbf{r}_p - A_{pv}A_{vv}^{-1}\mathbf{r}_v \end{cases} , \tag{28}$$

where, recalling the definitions of the related blocks ((42) and (43) in Appendix A), it can be observed that $B_{ww}, B_{pp} \succ 0$. Solution to (28) can be again computed by eliminating the unknown $\mathbf{g}_w$ from the first equation:

$$\mathbf{g}_w = B_{ww}^{-1}\left(\mathbf{r}_w - A_{wv}A_{vv}^{-1}\mathbf{r}_v - B_{wp}\mathbf{g}_p\right), \tag{29}$$

thus obtaining:

$$\left(B_{pp} - B_{pw}B_{ww}^{-1}B_{wp}\right)\mathbf{g}_p = \mathbf{r}_p - A_{pv}A_{vv}^{-1}\mathbf{r}_v - B_{pw}B_{ww}^{-1}\mathbf{r}_w + B_{pw}B_{ww}^{-1}A_{wv}A_{vv}^{-1}\mathbf{r}_v. \tag{30}$$

Equation (30) defines the 2^{nd}-level Schur complement:

$$C_{pp} = B_{pp} - B_{pw}B_{ww}^{-1}B_{wp}, \tag{31}$$

which can be indefinite according to the specific material properties and is generally non-symmetric. Of course, the 1^{st}- and 2^{nd}-level Schur complements, (27a) and (31), can be neither computed explicitly nor inverted. However, introducing approximations of A_{vv}^{-1}, B_{ww}^{-1}, and C_{pp}^{-1} into equations (25)-(30) can provide the vector $\mathbf{g}$ resulting from the application of some preconditioning operator $\mathbf{P}^{-1}$ to $\mathbf{r}$. The quality of such a preconditioner basically depends on the approximations chosen for these three blocks.

A_{vv} is an SPD linear combination of a stiffness and mass matrix (see eqs. (42a) and (43a)). As such, different effective algebraic approaches are already available from the literature, such as a classical incomplete triangular factorization:

$$A_{vv}^{-1} \simeq \widetilde{A}_{vv}^{-1} = \left[\text{ILU}(A_{vv})\right]^{-1}. \tag{32}$$

Since A_{vv} is SPD, the most effective ILU algorithm is the Incomplete Cholesky (IC) factorization. Other approaches are very appropriate as well, especially in view of the code extension to large-size problems and memory-distributed computational frameworks, such as advanced Algebraic Multigrid methods, e.g. [38–40]. Since our code is currently written at a Matlab prototypical level, to test the algorithmic capabilities of the proposed approach we simply rely on the approximation (32).

The matrix B_{ww} is the sum of the mass block A_{ww} with the product of a "mixed" stiffness and mass block. We compute this contribution through the Fixed-Stress (FS) algorithm:

$$B_{ww} \simeq \widetilde{B}_{ww} = A_{ww} - \text{FS}(A_{wv}A_{vv}^{-1}A_{vw}), \tag{33}$$

where the FS operator provides a diagonal or block-diagonal correction following the algebraic techniques introduced in [24]. The idea underlying the FS algorithm is to provide a lumped approximation of a matrix available in the general form $Q_1K^{-1}Q_2$, for some square SPD K and rectangular Q_1 and Q_2. If K is a stiffness matrix, the diagonal or block-diagonal entries of $\text{FS}(Q_1K^{-1}Q_2)$ are representative of the capability of deforming of the elements surrounding each node of the computational grid. From an algebraic point of view, we consider a set of m adjacent rows of Q_1, say $Q_1^{(i)}$, and the corresponding set of columns of Q_2, denoted as $Q_2^{(i)}$. The i-th $m \times m$ diagonal block of $\text{FS}(Q_1K^{-1}Q_2)$, $D^{(i)}$, is computed as:

$$D^{(i)} = r(Q_1^{(i)})K|_i^{-1}r(Q_2^{(i)}), \tag{34}$$

where $K|_i$ is the submatrix of K gathered from the entries located in the rows and columns corresponding to the position of the non-zero entries of $Q_1^{(i)}$ and $Q_2^{(i)}$, respectively (see Fig. 3 for a sketch of the $K|_i$ identification), and $r(\cdot)$ is a restriction operator on the submatrix within brackets retaining the non-zero entries only. The natural way to select m is to set $m = d$, i.e., we consider the block of rows corresponding to the physical unknowns associated to the same grid node, so that the position of the non-zero entries allows for reconstructing the graph of the connections with the surrounding nodes. Equation (34) cannot be safely used if either K is rank-deficient, because $K|_i$ could be singular, or the non-zero pattern of Q_2^T is different from Q_1, because $K|_i$ is generally rectangular. In order to be more general, we compute the entries $d^{(i)}$ of $D^{(i)}$ using an appropriate norm of $Q_1^{(i)}$, $Q_2^{(i)}$ and $K|_i$:

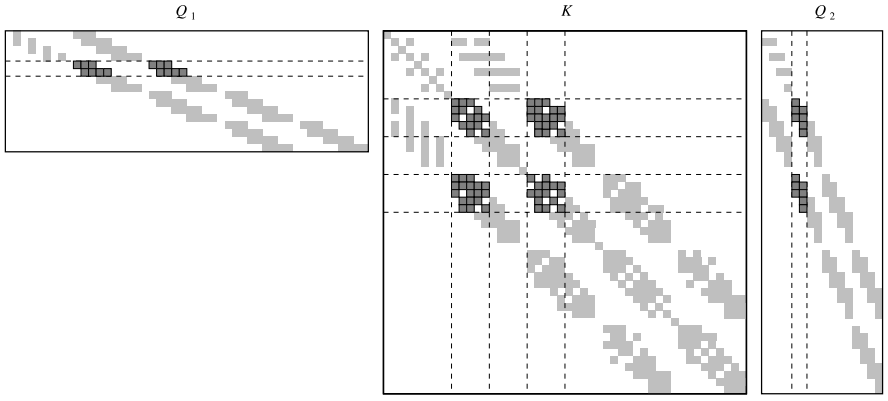

Fig. 3. Non-zero entries gathered from K in the approximation of $Q_1 K^{-1} Q_2$ according to the FS algorithm.

$$d^{(i)} = \frac{\|Q_1^{(i)}\| \, \|Q_2^{(i)}\|}{\|K|_i\|}, \tag{35}$$

for instance the 2-norm, as it is typically done in augmented Lagrangian approaches, e.g. [41].

Since $\widetilde{B}_{ww}$ is the sum of a mass matrix (A_{ww}) and a lumped approximation of $A_{wv}A_{vv}^{-1}A_{vw}$ through the FS algorithm, a good approximate application of this matrix is the inverse lumped one:

$$\widetilde{B}_{ww}^{-1} = \left[\text{lump}(\widetilde{B}_{ww})\right]^{-1}. \tag{36}$$

From a physical viewpoint, B_{ww} represents the stiffness matrix associated to the whole bulk made by both the solid part of the porous medium and the fluid. Actually, the solid stiffness matrix A_{vv} is modified isotropically by a volumetric component, which is consistent with the fluid deformation behavior.

Finally, the 2$^{\text{nd}}$-level Schur complement is the projection on the mass balance equation of the bulk compressibility effect. Therefore, the contribution in equation (31) depending on B_{ww}^{-1} has the physical meaning of an elastic storage term that can be approximated in the following way:

$$C_{pp} \simeq \widetilde{C}_{pp} = B_{pp} - (B_{pw}\widetilde{B}_{ww}^{-1}B_{wp}). \tag{37}$$

A classical incomplete triangular factorization or more advanced algebraic multigrid strategies are expected to provide effective approximations for the application of $\widetilde{C}_{pp}^{-1}$. In our code, we rely on a simple incomplete triangular factorization, as already done for $\widetilde{A}_{vv}^{-1}$:

$$\widetilde{C}_{pp}^{-1} \simeq \left[\text{ILU}(\widetilde{C}_{pp})\right]^{-1}. \tag{38}$$

B_{pp}, B_{pw} and B_{wp} depend on the inverse of A_{vv} in a similar way as B_{ww}, hence they can be computed by using Fixed-Stress (FS) operator:

$$B_{pp} \simeq \widetilde{B}_{pp} = A_{pp} - \text{FS}(A_{pv}A_{vv}^{-1}A_{vp}), \tag{39a}$$

$$B_{pw} \simeq \widetilde{B}_{pw} = A_{pw} - \text{FS}(A_{pv}A_{vv}^{-1}A_{vw}), \tag{39b}$$

$$B_{wp} \simeq \widetilde{B}_{wp} = A_{wp} - \text{FS}(A_{wv}A_{vv}^{-1}A_{vp}), \tag{39c}$$

Notice that in equations (39b) and (39c) the FS algorithm must be used with equation (35) only, because the involved rectangular blocks have different dimensions. The natural choice is to follow the unknowns associated to each grid node, i.e., each row of A_{pv} is associated with d adjacent columns of A_{vw} and each group of consecutive d rows of A_{wv} is associated to a single column of A_{vp}.

The construction and application of the resulting preconditioning operator $\mathbf{P}^{-1}$ is summarized in Algorithms 3.1 and 3.2, respectively. A left-preconditioned Bi-CGStab solver making use of $\mathbf{P}^{-1}$ is recalled in Algorithm 3.3.

Algorithm 3.1 PRECONDITIONER CONSTRUCTION $[\widetilde{A}_{vv}, \widetilde{B}_{ww}, \widetilde{C}_{pp}, \widetilde{B}_{pw}, \widetilde{B}_{wp}] = \text{cpt\_prc}(\mathbf{A})$.

1: $\widetilde{A}_{vv} = \text{ILU}(A_{vv})$;
2: $\widetilde{B}_{ww} = \text{lump}\left[A_{ww} - \text{FS}(A_{wv}A_{vv}^{-1}A_{wv})\right]$;
3: $\widetilde{B}_{pw} = A_{pw} - \text{FS}(A_{pv}A_{vv}^{-1}A_{vw})$;
4: $\widetilde{B}_{wp} = A_{wp} - \text{FS}(A_{wv}A_{vv}^{-1}A_{vp})$;
5: $\widetilde{C}_{pp} = \text{ILU}(A_{pp} - \text{FS}(A_{pv}A_{vv}^{-1}A_{vp}) - \widetilde{B}_{pw}\widetilde{B}_{ww}^{-1}\widetilde{B}_{wp})$;

Algorithm 3.2 PRECONDITIONER APPLICATION $[\mathbf{g}_v, \mathbf{g}_w, \mathbf{g}_p] = \text{app\_prc}(\mathbf{A}, \widetilde{A}_{vv}, \widetilde{B}_{ww}, \widetilde{C}_{pp}, \widetilde{B}_{pw}, \widetilde{B}_{wp}, \mathbf{r}_v, \mathbf{r}_w, \mathbf{r}_p)$.

$\mathbf{x}_v = \widetilde{A}_{vv}^{-1}\mathbf{r}_v$;
$\mathbf{s}_w = \mathbf{r}_w - A_{wv}\mathbf{x}_v$;
$\mathbf{t}_w = \widetilde{B}_{ww}^{-1}\mathbf{s}_w$;
$\mathbf{t}_p = \mathbf{r}_p - A_{pv}\mathbf{x}_v - \widetilde{B}_{pw}\mathbf{t}_w$;
$\mathbf{g}_p = \widetilde{C}_{pp}^{-1}\mathbf{t}_p$;
$\mathbf{y}_w = \widetilde{B}_{wp}\mathbf{g}_p$;
$\mathbf{x}_w = \widetilde{B}_{ww}^{-1}\mathbf{y}_w$;
$\mathbf{g}_w = \mathbf{t}_w - \mathbf{x}_w$;
$\mathbf{s}_v = A_{vw}\mathbf{g}_w + A_{vp}\mathbf{g}_p$;
$\mathbf{t}_v = \widetilde{A}_{vv}^{-1}\mathbf{s}_v$;
$\mathbf{g}_v = \mathbf{x}_v - \mathbf{t}_v$;

Algorithm 3.3 LEFT-PRECONDITIONED BLOCK BI-CGSTAB $[\mathbf{x}_v, \mathbf{x}_w, \mathbf{x}_p] = \text{block\_Bi-CGStab}(\mathbf{A}, \mathbf{b}_v, \mathbf{b}_w, \mathbf{b}_p, \varepsilon, k_{\max})$.

$[\mathbf{x}_v; \mathbf{x}_w; \mathbf{x}_p] = \mathbf{0}$;
$[\widetilde{A}_{vv}, \widetilde{B}_{ww}, \widetilde{C}_{pp}, \widetilde{B}_{pw}, \widetilde{B}_{wp}] = \text{cpt\_prc}(\mathbf{A})$;
$[\mathbf{r}_v, \mathbf{r}_w, \mathbf{r}_p] = \text{app\_prc}(\mathbf{A}, \widetilde{A}_{ww}, \widetilde{B}_{vv}, \widetilde{C}_{pp}, \widetilde{B}_{pv}, \widetilde{B}_{vp}, \mathbf{b}_v, \mathbf{b}_w, \mathbf{b}_p)$;
$\mathbf{r} = [\mathbf{r}_v; \mathbf{r}_w; \mathbf{r}_p]$;
$\mathbf{r}^* = \mathbf{r}$;
$\mathbf{p} = \mathbf{r}$;
$k = 0$;
$r_0 = \|\mathbf{r}\|_2$;
$r_k = \|\mathbf{r}\|_2 / r_0$;
$\rho_k = \mathbf{r}^T\mathbf{r}^*$;
while $r_k > \varepsilon$ & $k < k_{\max}$ **do**
  $k \leftarrow k + 1$;
  $[\mathbf{v}_v^*; \mathbf{v}_w^*; \mathbf{v}_p^*] = \mathbf{A}\mathbf{p}$;
  $[\mathbf{v}_v, \mathbf{v}_w, \mathbf{v}_p] = \text{app\_prc}(\mathbf{A}, \widetilde{A}_{vv}, \widetilde{B}_{ww}, \widetilde{C}_{pp}, \widetilde{B}_{pw}, \widetilde{B}_{wp}, \mathbf{v}_v^*, \mathbf{v}_w^*, \mathbf{v}_p^*)$;
  $\mathbf{v} = [\mathbf{v}_v; \mathbf{v}_w; \mathbf{v}_p]$;
  $\alpha = \rho_k / (\mathbf{v}^T\mathbf{r}^*)$;
  $\mathbf{s} = \mathbf{r} - \alpha\mathbf{v}$;
  $\mathbf{u}^* = \mathbf{A}\mathbf{s}$;
  $[\mathbf{u}_v, \mathbf{u}_w, \mathbf{u}_p] = \text{app\_prc}(\mathbf{A}, \widetilde{A}_{vv}, \widetilde{B}_{ww}, \widetilde{C}_{pp}, \widetilde{B}_{pw}, \widetilde{B}_{wp}, \mathbf{u}_v^*, \mathbf{u}_w^*, \mathbf{u}_p^*)$;
  $\mathbf{u} = [\mathbf{u}_v; \mathbf{u}_w; \mathbf{u}_p]$;
  $\omega = \mathbf{s}^T\mathbf{u} / (\mathbf{u}^T\mathbf{u})$;
  $[\mathbf{x}_v; \mathbf{x}_w; \mathbf{x}_p] \leftarrow [\mathbf{x}_v; \mathbf{x}_w; \mathbf{x}_p] + \alpha\mathbf{p} + \omega\mathbf{s}$;
  $\mathbf{r} = \mathbf{s} - \omega\mathbf{u}$;
  $r_k = \|\mathbf{r}\|_2 / r_0$;
  $\rho_{k+1} = \mathbf{r}^T\mathbf{r}^*$;
  $\beta = \rho_{k+1}\alpha / (\rho_k\omega)$;
  $\mathbf{p} \leftarrow \mathbf{r} + \beta\mathbf{p} - \omega\beta\mathbf{v}$;
end while

The overall cost for Algorithm 3.2 is roughly two ILU applications with size n_v, one ILU application with size n_p, three matrix-vector products with size $n_v \times n_p$, two matrix-vector products with size $n_v \times n_p$, two matrix-vector products with size $n_w \times n_p$ and two vector-vector products with size n_w.

4. Numerical examples

Three numerical examples have been analyzed to test the capability and efficiency of the proposed numerical model, which has been included in the GeoMatFem [27] Matlab research code for coupled solid-deformation and fluid-diffusion simulations. In all test cases, the inf-sup stable $\mathbb{Q}_2 - \mathbb{Q}_1$ Taylor-Hood discretization introduced in Appendix A, has been used. Furthermore, the incomplete factorizations required for A_{vv} and $\widetilde{C}_{pp}$ in the preconditioner construction, are computed with zero fill-in.

In the first example, the dynamic consolidation of a soil column is analyzed considering the compressibility of the individual phases. In the second one, wave propagation in a plane domain is studied, considering a layered soil characterized by an anisotropic constitutive model. In both cases, the results were compared using different space discretizations, time schemes and steps in order to verify the convergence and accuracy of these dynamic processes. Finally, wave splitting phenomena are investigated in an anisotropic and fully saturated porous material by considering the effect of a different degree of anisotropy between the solid phase and the mixture, through the Biot effective coefficient stress tensor. The purpose of this last example is twofold: first to demonstrate that is possible to capture this phenomenon due to the mechanical non-coaxiality of the solid medium, and second to show the robustness and efficiency of the updated coupled FEM code.

4.1. Dynamic consolidation of a soil column

The first benchmark, taken from [28], considers a column of fully saturated soil subjected to a harmonic load (Fig. 4). Unlike the

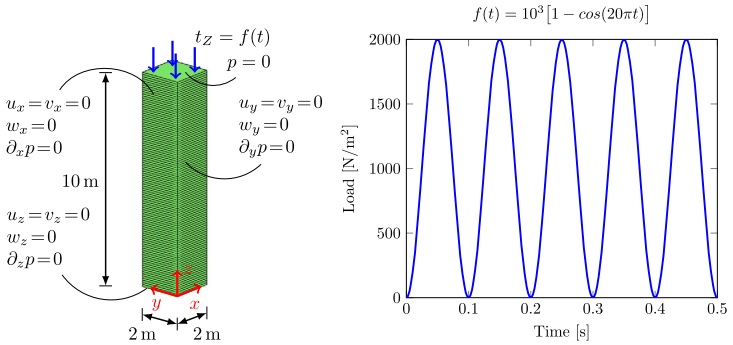

(a) Mesh and boundary conditions **(b)** External harmonic load

Fig. 4. Dynamic consolidation of a soil column.

Table 1
Soil column material parameters.

Parameter	Value	S.I. unit
E	14.52×10^6	Pa
ν	0.30	
φ_0	0.33	
K_s	6.05×10^9	Pa
K_F	2.20×10^9	Pa
k^r	10^{-2}	m/s
ρ_s	2000	kg/m^3
ρ_F	1000	kg/m^3

simulations in [42,28], here we account for the compressibility of both phases. All material parameters are given in Table 1. Two spatial discretizations, consisting of 100 (Fig. 4(a)) and 200 elements along the vertical direction, respectively, have been used, while two values of the parameter ϑ, equal to 1 (Backward Euler, B.E.) and 1/2 (Crank-Nicolson, C.N.), have been assumed by using a time step $\Delta t = 5 \cdot 10^{-4}$ s. The total number of degrees of freedom for the two grids is equal to $n = 5240$ and $n = 10440$, respectively.

Results, in terms of vertical displacement, solid and fluid velocity at the top surface of the column and fluid pore pressure on the bottom surface, are reported in Fig. 5. Both numerical analyses give the same results, with only a very slight difference smaller than 2% on the peak values of fluid velocity as an effect of the mesh size. The overall outcome is fully consistent with the results obtained for the same problem configuration in Reference [28]. Considering the Crank-Nicholson scheme, Fig. 6 shows the convergence profiles of the Left-preconditioned Block Bi-CGStab for four different time steps at the second Newton-Raphson iteration for both discretizations. A fast and stable convergence is appreciated with no significant deterioration due to the mesh refinement, despite the use of incomplete triangular factorization for the preconditioning of the inner blocks.

By this example, we can conclude that the two spatial discretizations with $\mathbb{Q}_2 - \mathbb{Q}_1$ Taylor-Hood elements provide accurate solutions for the dynamic analysis of a vertical soil column with compressible phases, as well as the time marching schemes with the selected time-step size.

4.2. Wave propagation in a 2D soil domain

In the second example, taken from [28] as well, a rectangular slice of soil in plane strain conditions is subjected to an impulsive load $f(t) = 10^5 \sin(25\pi t)[1 - H(t - \tau)]$, where $H(t - \tau)$ is the usual Heaviside function and $\tau = 0.04$ s is the duration of the impulse (Fig. 7). For this model, an elastic anisotropic constitutive law has been considered for both the solid phase (intrinsic) and the entire porous material (structural), with transversely isotropic elastic constants and assuming a horizontal plane of symmetry. This allows for the Biot effective stress coefficient tensor to be considered a diagonal matrix as usual. Furthermore, an anisotropic permeability tensor has been adopted, with higher permeability coefficients along the horizontal direction. All the material parameters are given in Tables 2 and 3.

The wave propagation analysis has been carried out by considering different discretizations of the plane domain, from a coarse mesh of 21×20 elements to a fine mesh of 168×160 elements. Two types of time-marching schemes (B.E. and C.N.) and three different time increments have been adopted.

Numerical results are reported in Fig. 8, using a constant time step $\Delta t = 1 \times 10^{-3}$ s and the C.N. scheme. No variation can be noted in the vertical displacement for the corner node C under the impulsive load as the mesh is refined, while the vertical velocity appears to be less accurate in the coarsest discretization. Again, the most sensitive variable to the grid size is the fluid velocity, especially at

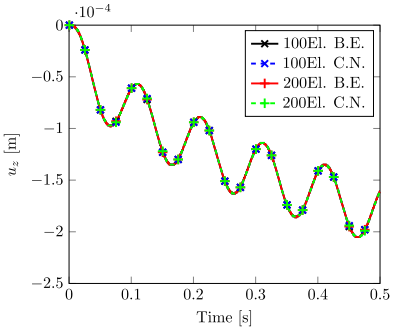

(a) Compaction

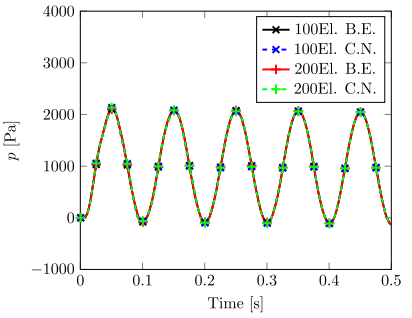

(b) Pore pressure at the bottom surface

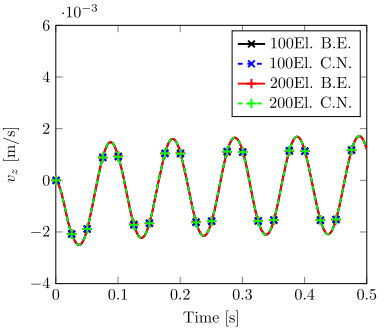

(c) Solid velocity at top surface

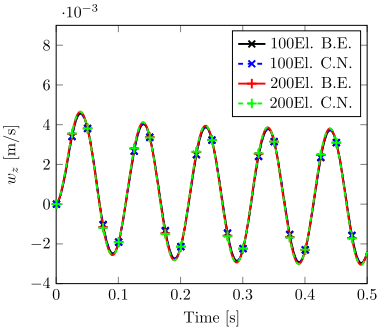

(d) Fluid velocity at top surface

Fig. 5. Dynamic consolidation results of a soil column.

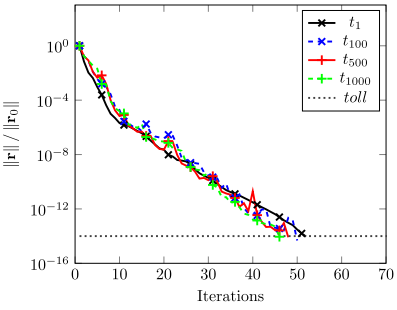

(a) Convergence profile, 100El. C.N.

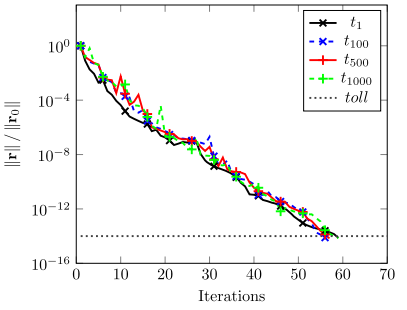

(b) Convergence profile, 200El. C.N.

Fig. 6. Convergence profiles for the dynamic consolidation of a soil column ($toll = 10^{-14}$).

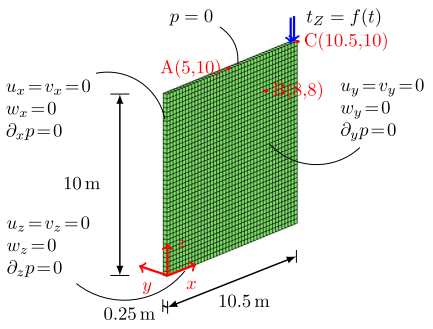

(a) Mesh and boundary conditions

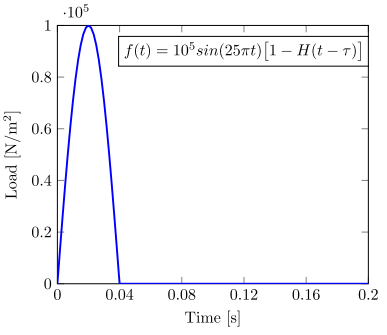

(b) External impulsive load

Fig. 7. Plane strain model.

Table 2
Plane strain problem material parameters.

Parameter	Value	S.I. unit
E_x, E_y	15.00×10^6	Pa
E_z	9.00×10^6	Pa
ν_{xy}, ν_{yx}	0.25	
ν_{yz}, ν_{xz}	0.30	
ν_{zx}, ν_{zy}	0.18	
$G_{xy} = \frac{E_x}{2(1+\nu_{xy})}$	6.00×10^6	Pa
G_{yz}, G_{xz}	3.60×10^6	Pa
n_0^F	0.33	
k_x^F, k_y^F	10^{-2}	m/s
k_z^F	10^{-4}	m/s
ρ_s	2000	kg/m^3
ρ_F	1000	kg/m^3
K_F	2.20×10^9	Pa

Table 3
Solid phase material parameters.

Parameter	Value	S.I. unit
E_x, E_y	3.0×10^7	Pa
E_z	1.8×10^7	Pa
ν_{xy}, ν_{yx}	0.25	
ν_{yz}, ν_{xz}	0.30	
ν_{zx}, ν_{zy}	0.18	
G_{xy}	1.2×10^7	Pa
G_{yz}, G_{zx}	7.2×10^6	Pa

the peak values. In Fig. 8(b), the pore pressure evolution for the internal node B is also shown. Only the coarse mesh provides higher pressure peaks (4÷6%) than the other grids.

Fig. 9(a) and 9(b) show the plane motion and fluid velocity at node A. In the first panel, it can be seen that all meshes give the same result except for the coarsest, which differs by about 6% in some time steps, while the difference between the models is more evident in the fluid velocity. Considering the 84×80 elements discretization, Fig. 9(c) and 9(d) show the behavior of the previous main variables for different time schemes and steps. In both graphs, by adopting the B.E. scheme and decreasing the time increments, $\Delta t = 2\times10^{-3}$ s, 1×10^{-3} s and 5×10^{-4} s (indicated in the legend as "2", "1" and "05"), the solid motion and the speed of fluid increase. Differently, taking the C.N. scheme and varying the time steps, the solution curves remain unchanged and are larger than the previous ones. B.E. scheme's stiff results, also explained in [17], are due to its artificial damping, not present in the C.N. scheme, which provides accurate results also with relatively large time steps.

In Fig. 10 the amplified deformed mesh and the Euclidean norm of soil displacements are reported at four different time steps with the finest mesh (168×160 elements). By this graphic representation, the propagation of the body and surface waves, from the impulsive load to the opposite boundary, are clearly visible.

Finally, Fig. 11 shows the convergence profiles for all the different discretizations, obtained with the C.N. scheme, at given time steps. Though a detrimental effect of the mesh refinement can be now appreciated, convergence is still satisfactorily fast and stable throughout the full transient simulation for any grid.

In this example, plane wave propagation in a transverse isotropic porous material has been well reproduced. The model consistency and stability have been verified by both progressive space and time grid refinements. All the results for this example are consistent with the outcome obtained in [28].

4.3. 3D wave propagation

In this section, wave propagation and shear wave splitting, arising from an impulsive source, in a 3D anisotropic soil domain have been reproduced and investigated. In general, the splitting phenomenon occurs when a polarized shear wave hits an anisotropic medium and thus splits into two waves of different speed and orientation. In our case, specifically, we are interested in numerically studying this phenomenon in the particular situation of non-coaxiality between the mechanical properties of the single solid phase and the entire porous medium, which will generate a coupling between the volumetric and deviatoric stresses of the mixture, and in turn create different shear waves.

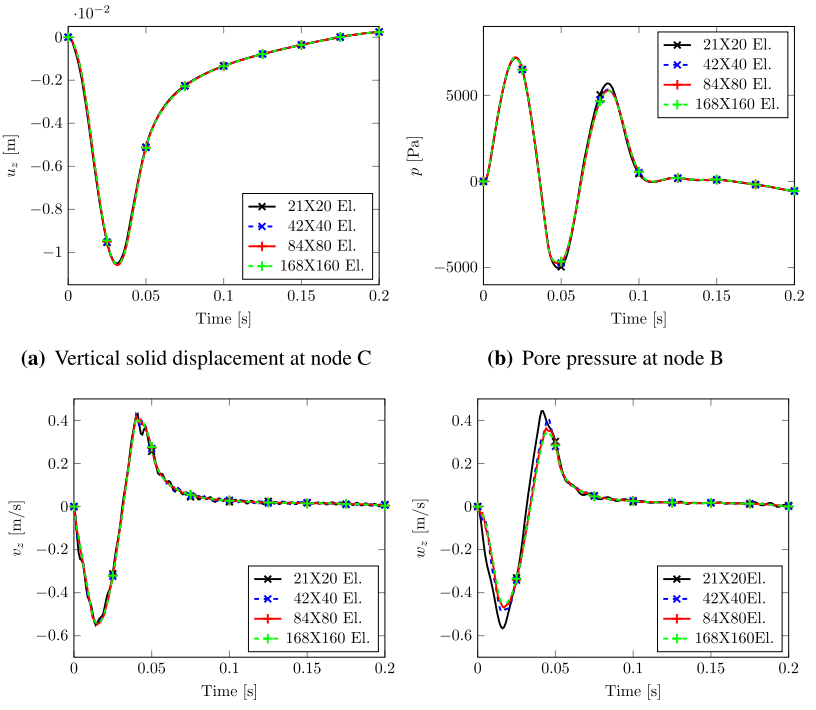

(a) Vertical solid displacement at node C

(b) Pore pressure at node B

(c) Vertical solid velocity at node C

(d) Vertical fluid velocity at node C

Fig. 8. Wave propagation results for different discretizations of the 2D soil domain.

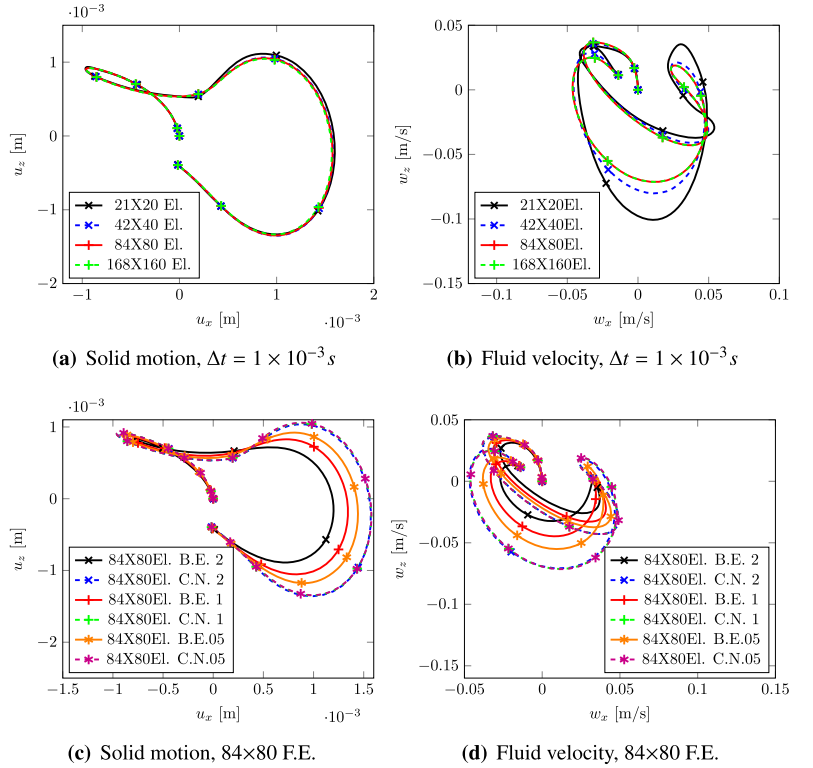

(a) Solid motion, $\Delta t = 1 \times 10^{-3} s$

(b) Fluid velocity, $\Delta t = 1 \times 10^{-3} s$

(c) Solid motion, 84×80 F.E.

(d) Fluid velocity, 84×80 F.E.

Fig. 9. Node A results for different discretizations, time schemes and steps.

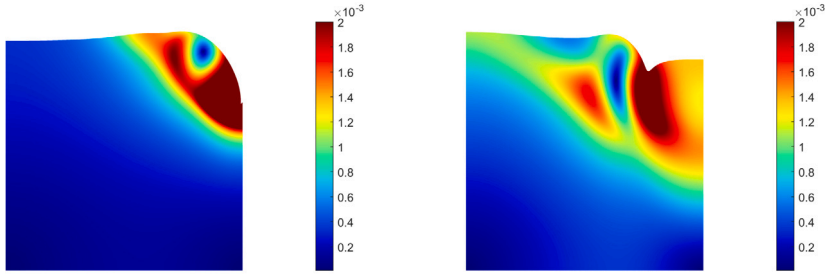

(a) t = 0.05 s **(b)** t = 0.1 s

(c) t = 0.15 s **(d)** t = 0.20 s

Fig. 10. Deformed mesh (amplified by scale factor 500) and contour of the norm of soil displacements $\|\mathbf{u}\| = \sqrt{u_x^2 + u_z^2}$ for 2D domain. (For interpretation of the colors in the figure(s), the reader is referred to the web version of this article.)

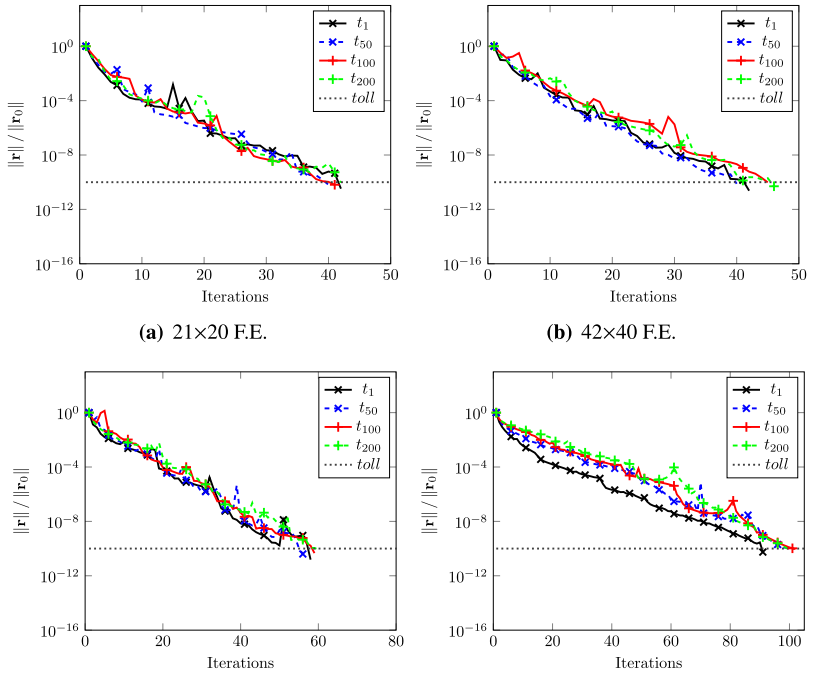

(a) 21×20 F.E. **(b)** 42×40 F.E.

(c) 84×80 F.E. **(d)** 168×160 F.E.

Fig. 11. Convergence profiles for different discretizations of the 2D soil domain ($toll = 10^{-10}$).

We consider the square soil prism shown in Fig. 12, consisting of a transversely isotropic soil with the material properties of the previous 2D example (Tables 2 and 3) and an isotropic 2-m thick surface layer. The impulsive source is a concentrated vertical pressure of $I = 2546.5\,\mathrm{Ns/mm^2}$ positioned between the two soil layers and applied in 1 $\mathrm{m^2}$ around point A. The analysis time in this

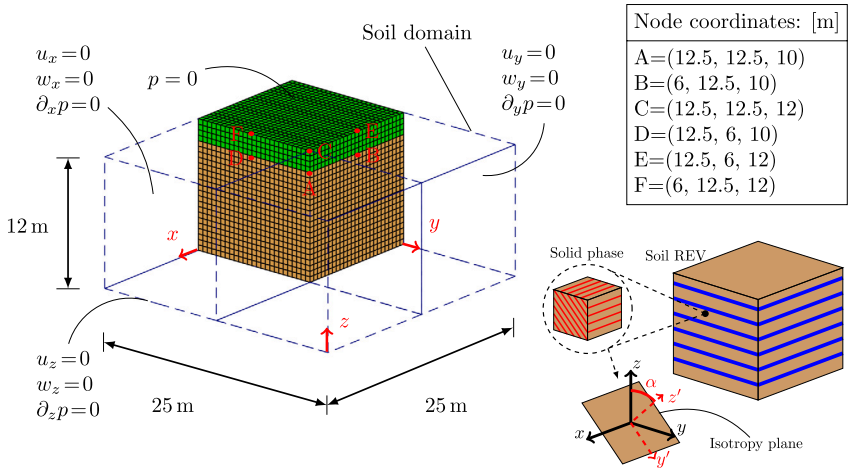

Fig. 12. 3D soil model.

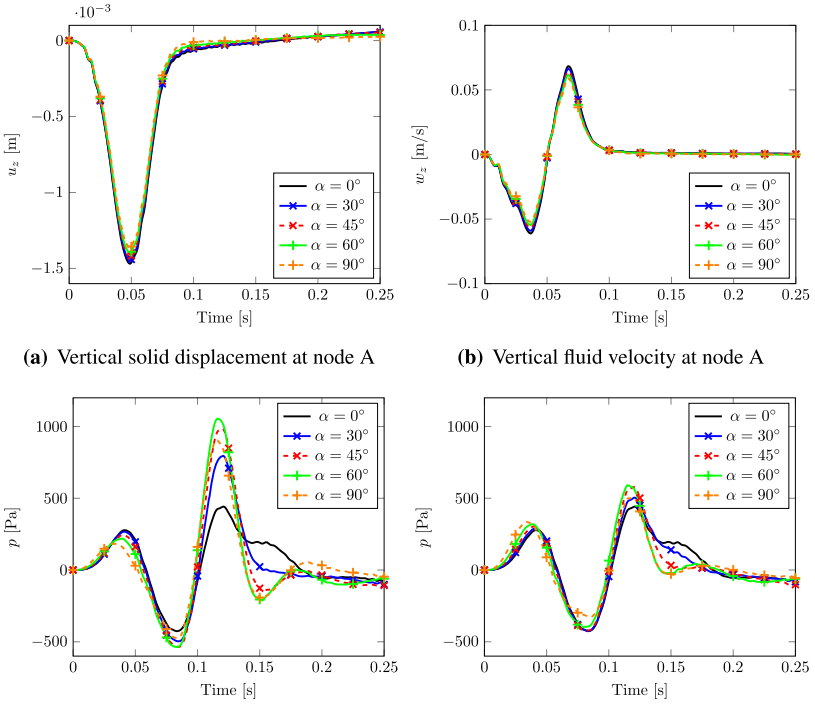

(a) Vertical solid displacement at node A

(b) Vertical fluid velocity at node A

(c) Pore pressure at node D

(d) Pore pressure at node B

Fig. 13. Wave propagation results in 3D soil domain under varying rotation of the intrinsic isotropic plane of solid phase.

case is 0.25 s. As for the boundary conditions, soil displacements and fluid velocities orthogonal to the lateral and bottom surfaces are precluded and a zero pore fluid pressure is also prescribed on the top surface.

A set of analyses has been carried out by rotating the intrinsic isotropic plane of the solid phase along the X direction (see schematic REV in Fig. 12), in order to catch the shear wave splitting phenomenon that arises from the different degree of anisotropy between the solid phase and the entire porous skeleton, accounted for by the Biot coefficient stress tensor. When the intrinsic isotropic plane is horizontal or orthogonal to the Y axis, it is possible to restrict the domain to one quarter only of the full porous prismatic volume. By distinction, when the intrinsic isotropic plane is rotated, it can be necessary to use half or even the whole volume, if a generic inclination is assumed. Therefore, we need to use different models of increasing size.

In Fig. 13, the time evolution of some variables of interest is plotted as the rotation angle α of the intrinsic isotropic plane changes. Considering the vertical displacement of the point directly above the impulsive load (node C), just a small variation of u_z, equal to about 7%, can be noticed on the peak value (Fig. 13(a)). As for the vertical fluid velocities at the same node C, the vertical displacements are slightly less pronounced but aligned with those obtained with the reference value $\alpha = 0°$ (Fig. 13(b)). In the two

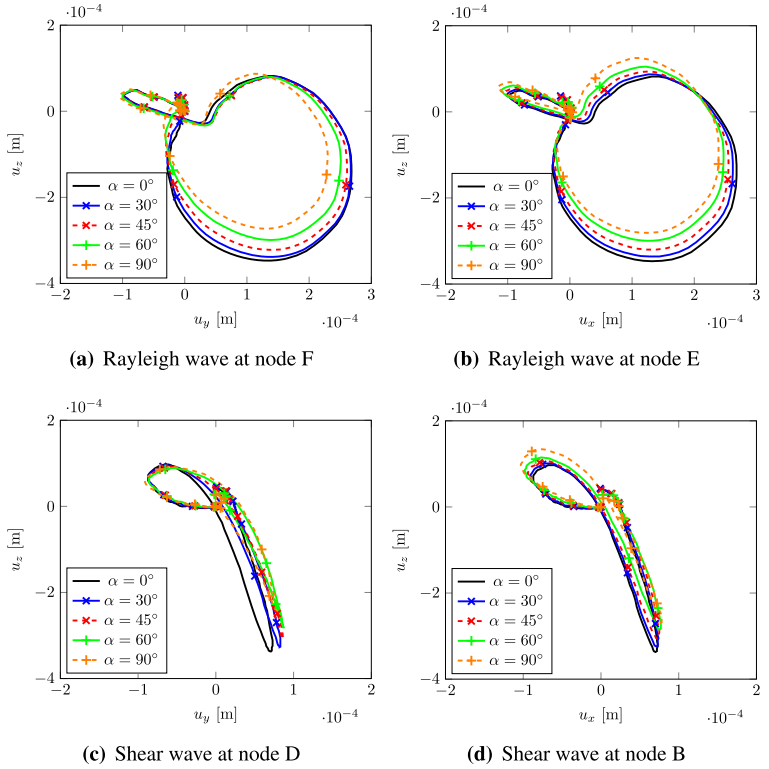

(a) Rayleigh wave at node F

(b) Rayleigh wave at node E

(c) Shear wave at node D

(d) Shear wave at node B

Fig. 14. Wave splitting for 3D soil domain.

bottom frames Fig. 13(c) and 13(d), the pore pressure evolution for the two nodes B and D are shown. No rotation ($\alpha = 0°$) produces the same pressure diagram (black line) in both nodes, while different diagrams with higher pressure peaks are obtained when α is varied.

Fig. 14, which plots the plane motion of four nodes belonging to the orthogonal directions X and Y, is particularly meaningful to analyze the wave splitting effect. In the two top frames, the nearly circular shape describes the typical Rayleigh waves (plane motion on solid surface) of the opposite nodes F and E, as a result of the combination of shear and pressure waves incident on the surface of the medium. In contrast, the two bottom frames represent the typical motion due to shear waves orthogonal to the direction of propagation. It can be observed that, with no rotation of the intrinsic isotropic plane, the motions of the nodes are the same (black line). However, as α changes, the waves take different shapes between the two directions. The rotation of the intrinsic isotropic plane induces a larger stiffness reduction along the Y direction, given the smaller stress state and reduced displacements. This important result computationally demonstrates the shear wave splitting that arises from a different degree of anisotropy between the solid phase and the porous matrix.

Fig. 15 illustrates the amplified deformed mesh and Euclidean norm of solid displacements at six different times. This allows the wave propagation, due to an impulsive loading on the porous medium, to be visualized graphically. Shear and Rayleigh waves move faster and with greater amplitude along the X direction.

In Fig. 16, the sparsity pattern for two different 3D discretizations, i.e., the finest and the intermediate mesh, are shown together with the corresponding convergence profiles of the linear solver with $\alpha = 0°$ and $\alpha = 45°$. In order to improve the efficiency of the incomplete triangular factorizations, the nodal numbering in each mesh is reordered by a geometric sorting algorithm, so as to reduce the bandwidth of the stiffness blocks $K_{\alpha\beta}$. Also in these 3D complex dynamic coupled analyses, the proposed preconditioned iterative solver always exhibits a fast and robust behavior, reaching the exit criterion in few iterations (37 and 39 on average for two discretizations, respectively).

In summary, the numerical model here discussed is able to represent the propagation of seismic waves in the 3D space of a saturated anisotropic porous medium and to simulate the phenomenon of shear wave splitting, also in the particular case of non-coaxiality of the mechanical properties between the solid phase and the entire solid skeleton. Furthermore, by using a suitable spatial and temporal discretization, the code demonstrates its robustness providing stable and accurate results.

5. Solver performance

The computational efficiency of the linear solver has been investigated in more detail as compared to the available default Matlab algorithm ("backslash", \). Numerical tests have been performed on a standard desktop workstation, equipped with an Intel(R) Core(TM) i7-9800X processor with 3.80 GHz (CPU) and 32.0 GB of RAM for serial simulations. In Table 4, the performance of the

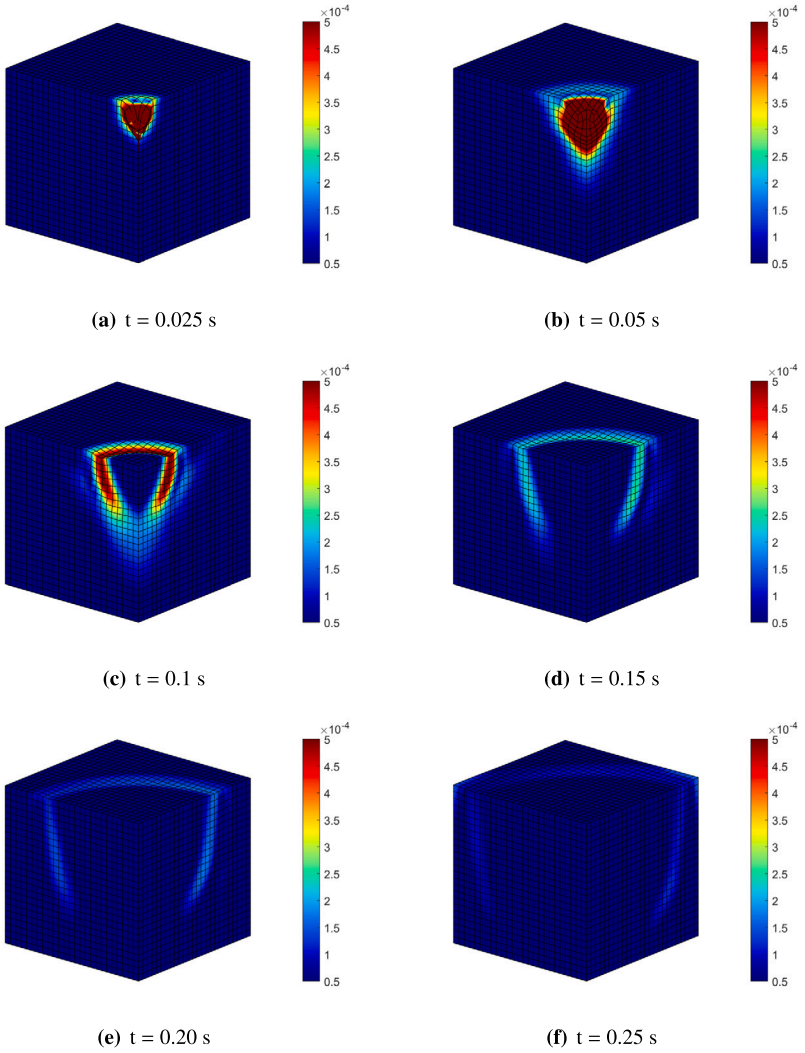

(a) t = 0.025 s **(b)** t = 0.05 s

(c) t = 0.1 s **(d)** t = 0.15 s

(e) t = 0.20 s **(f)** t = 0.25 s

Fig. 15. Deformed mesh (amplified by scale factor 500) and contour of the norm of soil displacements $\|\mathbf{u}\| = \sqrt{u_x^2 + u_y^2 + u_z^2}$ for 3D domain.

left preconditioned Bi-CGStab solver has been summarized. As expected, in the case of 1D and 2D relatively small models, Matlab (\) solver either outperforms or is roughly comparable to our iterative method. However, in 3D models the use of preconditioned iterations is mandatory. Notice that even our prototypical Matlab implementation run on a standard desktop PC is able to solve 3D coupled models with up to 1.2 million unknowns, while the \ direct solver fails for memory issues at about 300000 unknowns. These results, along with the algorithmic robustness shown in all numerical experiments, provide evidence that the proposed approach appears to be very promising for a future high-performance implementation.

A thorough theoretical analysis of the properties of the proposed preconditioner is not easy because the global block system matrix $\mathbf{A}$ does not possess any clear structure. Therefore, the quality of the preconditioner has been experimentally assessed by comparing the eigenspectrum of the native system matrix $\mathbf{A}$ and that of the preconditioned matrix $\mathbf{P}^{-1}\mathbf{A}$. For this analysis we consider a coarser discretization made of $12 \times 12 \times 12$ F.E., similar to the model in Fig. 12 and totaling 8281 nodes and 30212 dof. Fig. 17(a) and the upper part of Table 5 provide evidence of the pronounced non-symmetric nature of $\mathbf{A}$, which has two clear eigenvalue clusters largely apart one from the other (around 10^{-6} and 10^{5}, respectively) and very large imaginary parts (up to about 10^{4}). By distinction, the eigenspectrum of the preconditioned matrix $\mathbf{P}^{-1}\mathbf{A}$ (Fig. 17(b) and lower part of Table 5) is very well clustered between 0.04 and 1, with almost negligible imaginary parts around 10^{-3}. It is well-known that the convergence of non-symmetric solvers depends not only on the eigenvalues of the preconditioned matrix, but also on the properties of the eigenvectors. The numerical experience, however, shows that a preconditioned matrix with a clustered eigenspectrum sufficiently far from 0 rarely provides unsatisfactory results. Hence, the outcome shown here appears to be quite promising for the proposed approach.

The solver robustness is investigated by a sensitivity analysis on: (i) the rotation α of the axis of the transverse anisotropy constitutive model, and (ii) the type of anisotropic elastic constitutive model. We still consider the 3D wave propagation problem, but now use a mesh refinement corresponding to $21 \times 42 \times 20$ F.E., which totals 295552 dof. Fig. 18(a) plots the total solution time

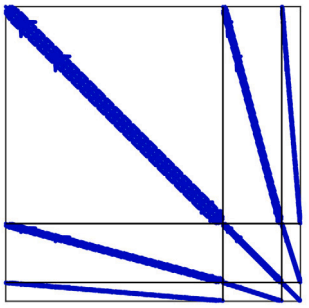

(a) System Matrix for 25×25×24 mesh

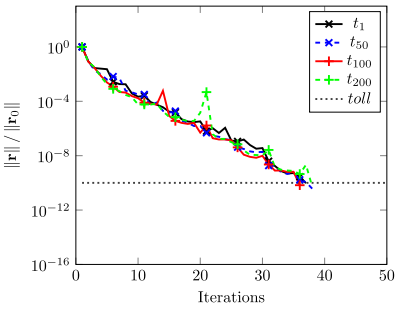

(b) Residual's diagram for 25×25×24 mesh

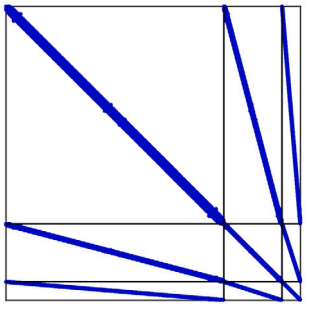

(c) System Matrix for 25×50×24 mesh

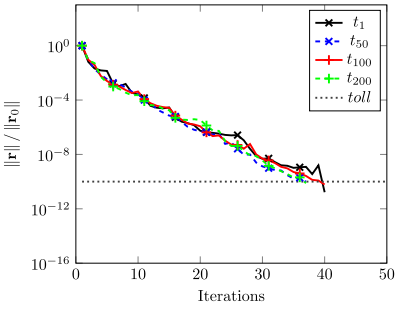

(d) Residual's diagram for 25×50×24 mesh

Fig. 16. Pattern and convergence profile for two different 3D discretizations ($toll = 10^{-10}$).

Table 4
Left preconditioned Bi-CGStab solver performance.

Case	Mesh	Nodes	dof_{tot}	CPU Time [s]	
				Bi-CGStab	Matlab (\)
1D	1×1×100	1208	2000	0.12	0.02
1D	1×1×200	2408	4000	0.19	0.04
2D	1×21×20	3148	8552	1.50	0.69
2D	1×42×40	12173	33969	5.67	3.85
2D	1×84×80	47863	142028	36.21	65.14
2D	1×168×160	189803	566384	665.46	960.01
3D	12×12×12	8281	30212	55.24	1011.54
3D	21×21×20	39248	148804	74.29	1303.28
3D	25×25×24	65624	254224	276.69	1932.60
3D	21×42×20	77153	295552	325.86	–
3D	25×50×24	129349	504124	735.05	–
3D	42×42×20	151661	586948	956.24	–
3D	50×50×24	254949	999649	2663.80	–
3D	42×42×40	297861	1159788	3367.95	–

of the linear system with respect to different rotations of the isotropic symmetry plane. Two scenarios are considered, namely the rotation of the isotropic plane of the solid matrix (red profile) and the rotation of the isotropic plane of the entire porous matrix (blue profile). In both scenarios, a variation of α causes a relatively small impact on both the total solution time and iteration count. The variation is at most equal to 7% for $\alpha = 45°$ in the case of non coaxiality of the porous matrix and 17% for the rotation of the material axes of the entire porous medium at the same angle.

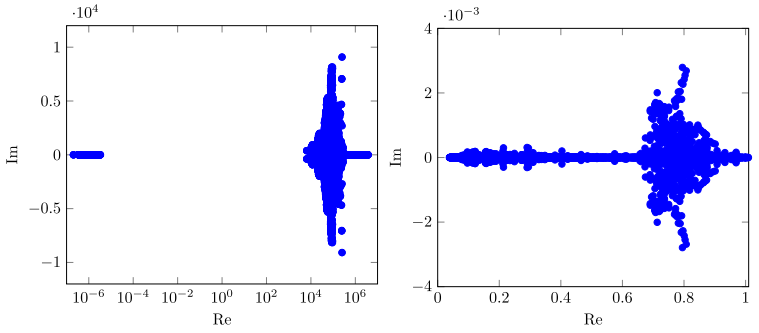

(a) Eigenvalues of original matrix. **(b)** Eigenvalues of the preconditioned matrix.

Fig. 17. Eigenvalue distribution for a 12×12×12 3D mesh.

Table 5
Extreme eigenvalues for a $12 \times 12 \times 12$ 3D mesh.

Eigenvalues	Re part	Im part
$\lambda(\mathbf{A})_{Xmin}$	2.0391×10^{-7}	0.0
$\lambda(\mathbf{A})_{Xmax}$	3.7633×10^{6}	0.0
$\lambda(\mathbf{A})_{Ymax}$	2.5166×10^{5}	9.0827×10^{3}
$\lambda(\mathbf{P}^{-1}\mathbf{A})_{Xmin}$	0.0381	0.0
$\lambda(\mathbf{P}^{-1}\mathbf{A})_{Xmax}$	1.0409	0.0
$\lambda(\mathbf{P}^{-1}\mathbf{A})_{Ymax}$	0.7949	0.0028

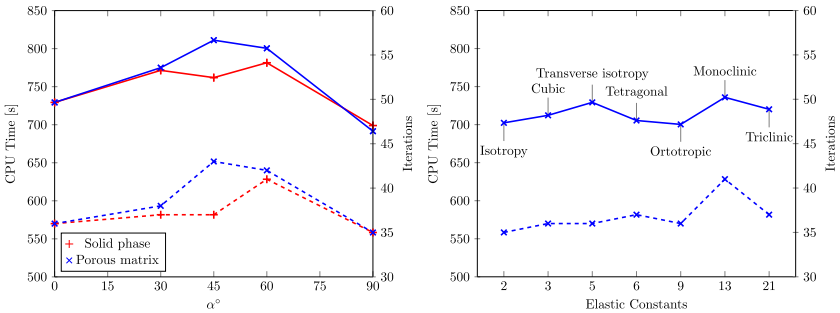

(a) Isotropic plane rotations **(b)** Anisotropic constitutive model

Fig. 18. CPU time solution (continuous line) and number of iterations (dashed line) with respect to anisotropy.

A similar outcome is obtained by varying the type of anisotropic elastic constitutive model (Fig. 18(b)). Employing 7 different behaviors for the porous medium (the same type of anisotropy has been assumed for the solid phase), solution times and iteration counts are shown as a function of the corresponding number of independent elastic constants. Horizontal axis has been built starting from the isotropic material, with two elastic parameters $E = 12.00 \times 10^6 Pa$ and $\nu = 0.3$. Then, the cubic model has 3 independent parameters E, ν, G, the transversely isotropic depends on 5 parameters (Tables 2 and 3), up to models where the number of elastic symmetries (see [16] for further details) is reduced until the triclinic material, which requires 21 different parameters for the description of its mechanical behavior. Also from this analysis, it can be appreciated that the solver is very marginally affected by the variation of the constitutive model and is able to solve the linear system on average in the same time, at most with a 5% difference. Notice that there was no need of operating on the parameters of the selected inner preconditioners, such as the triangular factorizations. All the test cases have been solved by simply assuming zero fill-in for both the IC and ILU factorizations used for A_{vv} and $\widetilde{C}_{pp}$, respectively.

All the tests above highlight the robustness of the proposed approach, which is able to solve effectively the problem at hand with approximately the same computational effort, regardless of the rotation of the isotropic plane and the type of constitutive model.

6. Conclusion

In this work, a multi–field coupled dynamic model for anisotropic porous materials has been developed and implemented. The mathematical formulation accounts for the intrinsic and macroscopic constitutive property of the poro–elastic material, through an extension of Terzaghi's stress principle. The numerical solution to the governing coupled PDEs is obtained by using a FEM framework together with the implicit monolithic ϑ–method as a time-marching scheme.

A significant issue for this type of model, which often limits its use in practical 3D applications, relies on the coupled multi–physical nature of the resulting discretized system of equations that require ad hoc solver developments for large-size 3D applications. In this work, a specific preconditioned iterative algorithm, used for solution of the ill-conditioned multi–block non–symmetric systems that arise from the selected discretization spaces, is presented. The application of the proposed algorithm turns out to be robust and computationally efficient even in the prototypical Matlab implementation tested herein, allowing for the solution on a standard desktop PC of complex 3D models with up to 1.2 million unknowns. Numerical applications have been analyzed to investigate the shear wave splitting phenomenon in a 3D anisotropic soil setting. The results show the capabilities and the potential of the proposed numerical model for complex multi–field dynamic simulations. Further work is ongoing to move from the current prototypical Matlab implementation of the GeoMatFem research code to a high-performance version.

CRediT authorship contribution statement

Nico De Marchi: Formal analysis, Investigation, Methodology, Software, Validation, Writing – original draft, Conceptualization, Writing – review & editing. **Giovanna Xotta:** Investigation, Conceptualization, Methodology, Software, Writing – original draft, Writing – review & editing. **Massimiliano Ferronato:** Conceptualization, Methodology, Software, Supervision, Writing – original draft, Writing – review & editing, Investigation. **Valentina Salomoni:** Project administration, Conceptualization, Funding acquisition, Supervision.

Declaration of competing interest

The authors declare that they have no known competing financial interests or personal relationships that could have appeared to influence the work reported in this paper.

Data availability

No data was used for the research described in the article.

Acknowledgements

Financial support from the Italian Ministry of University and Research (MUR), in the framework of PRIN2017 #2017HFPKZY and PRIN2020 #20209F3A37 Projects, is gratefully acknowledged. M.F. is a member of the Gruppo Nazionale Calcolo Scientifico - Istituto Nazionale di Alta Matematica (GNCS-INdAM).

Appendix A

A.1. Finite element details

A Finite Element approach is used to approximate the weak form (11) of the coupled dynamic differential equations for a fully saturated porous material. The following approximations $\boldsymbol{u}^h$, $\boldsymbol{v}^h$, $\boldsymbol{w}^h$, p^h are introduced for the unknown fields:

$$\boldsymbol{u}^h = \sum_{i=1}^{n_u} \boldsymbol{\psi}_i(\boldsymbol{x}) u_i(t), \quad \boldsymbol{v}^h = \sum_{i=1}^{n_v} \boldsymbol{\psi}_i(\boldsymbol{x}) v_i(t), \quad \boldsymbol{w}^h = \sum_{j=1}^{n_w} \boldsymbol{\phi}_j(\boldsymbol{x}) w_j(t), \quad p^h = \sum_{i=k}^{n_p} \eta_k(\boldsymbol{x}) p_k(t), \tag{40}$$

where n_u, n_v, n_w, and n_p denote, respectively, the number of degrees of freedom for the displacements (u_i), solid velocities (v_i), fluid velocities (w_j), and pressures (p_k), collected in the vectors $\mathbf{u} \in \mathbb{R}^{n_u}$, $\mathbf{v} \in \mathbb{R}^{n_v}$, $\mathbf{w} \in \mathbb{R}^{n_w}$, and $\mathbf{p} \in \mathbb{R}^{n_p}$. The vector functions $\boldsymbol{\psi}_i$, $\boldsymbol{\phi}_j$, and the scalar functions η_k are the basis for the finite element approximation spaces. For instance, a consistent inf-sup stable discretization is generated by $\mathbb{Q}_2 - \mathbb{Q}_1$ Taylor-Hood elements. By defining a partition $\mathcal{T}^h$ of Ω made of non-overlapping elements Ω^e, the basis functions in equation (40) can be set as follows:

$$\boldsymbol{\psi}_i \in S^h_{u,v}(\Omega) = \{\boldsymbol{\psi} \in \boldsymbol{H}^1(\Omega), \boldsymbol{\psi}|_{\Omega^e} \in [\mathbb{Q}_2(\Omega^e)]^d \ \forall \Omega^e \in \mathcal{T}^h\}, \qquad i = 1, \dots, n_v, \tag{41a}$$

$$\boldsymbol{\phi}_j \in S^h_w(\Omega) = \{\boldsymbol{\phi} \in \boldsymbol{H}(\mathrm{div}; \Omega), \boldsymbol{\phi}|_{\Omega^e} \in [\mathbb{Q}_1(\Omega^e)]^d \ \forall \Omega^e \in \mathcal{T}^h\}, \qquad j = 1, \dots, n_w, \tag{41b}$$

$$\eta_k \in S^h_p(\Omega) = \{\eta \in H^1(\Omega), \eta|_{\Omega^e} \in \mathbb{Q}_1(\Omega^e) \ \forall \Omega^e \in \mathcal{T}^h\}, \qquad k = 1, \dots, n_p, \tag{41c}$$

with $\mathbb{Q}_1(\Omega^e)$ and $\mathbb{Q}_2(\Omega^e)$ the space of d-linear and d-quadratic polynomials in Ω^e, respectively. With the space selection (41), we have $n_u = n_v$, $n_v > n_w$, and $n_p < n_w$ ($n_p = n_w/d$).

By introducing the approximations (40) into the weak form (11) and replacing the continuous with the discrete spaces (41), we obtain the system of 1st order differential equations in time (13). The internal blocks in $\mathbf{M}$ and $\mathbf{K}$ of (14) consist of I_u, i.e., the identity in $\mathbb{R}^{n_u \times n_u}$, and:

$$[M_{vv}]_{ij} = (\boldsymbol{\psi}_i, \rho^S \boldsymbol{\psi}_j)_\Omega, \qquad i = 1, \dots, n_v, \quad j = 1, \dots, n_v, \tag{42a}$$

$$[M_{vw}]_{ij} = (\boldsymbol{\psi}_i, \rho^F \boldsymbol{\phi}_j)_\Omega, \qquad i = 1, \dots, n_v, \quad j = 1, \dots, n_w, \tag{42b}$$

$$[M_{ww}]_{ij} = (\boldsymbol{\phi}_i, \rho_F \boldsymbol{\phi}_j)_\Omega, \qquad i = 1, \dots, n_w, \quad j = 1, \dots, n_w, \tag{42c}$$

$$[M_{pw}]_{ij} = (\eta_i, \operatorname{div} \frac{\boldsymbol{k}^F}{g} \boldsymbol{\phi}_j)_\Omega, \qquad i = 1, \dots, n_p, \quad j = 1, \dots, n_w, \tag{42d}$$

$$[M_{pp}]_{ij} = (\eta_i, \Lambda \eta_j)_\Omega, \qquad i = 1, \dots, n_p, \quad j = 1, \dots, n_p; \tag{42e}$$

and:

$$[K_{vu}]_{ij} = (\nabla^s \boldsymbol{\psi}_i, \mathbf{C} : \nabla^s \boldsymbol{\psi}_j)_\Omega, \qquad i = 1, \dots, n_v, \quad j = 1, \dots, n_u, \tag{43a}$$

$$[K_{vp}]_{ij} = -(\nabla^s \boldsymbol{\psi}_i, \boldsymbol{A} \eta_j)_\Omega, \qquad i = 1, \dots, n_v, \quad j = 1, \dots, n_p, \tag{43b}$$

$$[K_{wv}]_{ij} = -(\boldsymbol{\phi}_i, \varphi \gamma_F \boldsymbol{k}^{F,-1} \boldsymbol{\psi}_j)_\Omega, \qquad i = 1, \dots, n_w, \quad j = 1, \dots, n_v, \tag{43c}$$

$$[K_{ww}]_{ij} = (\boldsymbol{\phi}_i, \varphi \gamma_F \boldsymbol{k}^{F,-1} \boldsymbol{\phi}_j)_\Omega, \qquad i = 1, \dots, n_w, \quad j = 1, \dots, n_w, \tag{43d}$$

$$[K_{wp}]_{ij} = -(\operatorname{div} \boldsymbol{\phi}_i, \eta_j)_\Omega, \qquad i = 1, \dots, n_w, \quad j = 1, \dots, n_p, \tag{43e}$$

$$[K_{pv}]_{ij} = (\eta_i, \boldsymbol{A} : \nabla^s \boldsymbol{\psi}_j)_\Omega, \qquad i = 1, \dots, n_p, \quad j = 1, \dots, n_v, \tag{43f}$$

$$[K_{pp}]_{ij} = (\nabla \eta_i, \frac{\boldsymbol{k}^F}{\gamma_F} \nabla \eta_j)_\Omega, \qquad i = 1, \dots, n_p, \quad j = 1, \dots, n_p; \tag{43g}$$

References

[1] W. Ehlers, J. Bluhm, Porous Media: Theory, Experiments and Numerical Applications, Springer Science & Business Media, 2002.
[2] Z. Chen, G. Huan, Y. Ma, Computational Methods for Multiphase Flows in Porous Media, SIAM, 2006.
[3] J.I. Siddique, A. Ahmed, A. Aziz, C.M. Khalique, A review of mixture theory for deformable porous media and applications, Appl. Sci. 7 (9) (2017) 917.
[4] M. Mahanty, P. Kumar, A.K. Singh, A. Chattopadhyay, Dynamic response of an irregular heterogeneous anisotropic poroelastic composite structure due to normal moving load, Acta Mech. 231 (6) (2020) 2303–2321.
[5] H. Ding, L. Tong, C. Xu, Z. Cao, R. Wang, S. Li, On propagation characteristics of Rayleigh wave in saturated porous media based on the strain gradient nonlocal Biot theory, Comput. Geotech. 141 (2022) 104522.
[6] S. Nardean, M. Ferronato, A.S. Abushaikha, A block preconditioner for two-phase flow in porous media by mixed hybrid finite elements, Comput. Math. Methods 3 (6) (2021) e1207.
[7] Y. Ishii, S. Biwa, A. Kuraishi, Influence of porosity on ultrasonic wave velocity, attenuation and interlaminar interface echoes in composite laminates: finite element simulations and measurements, Compos. Struct. 152 (2016) 645–653.
[8] P. Martakis, G. Aguzzi, V.K. Dertimanis, E.N. Chatzi, A. Colombi, Nonlinear periodic foundations for seismic protection: practical design, realistic evaluation and stability considerations, Soil Dyn. Earthq. Eng. 150 (2021) 106934.
[9] M. Hodaei, P. Maghoul, N. Wu, Three-dimensional biomechanical modeling of cylindrical bone-like porous materials subject to acoustic waves, Int. J. Mech. Sci. 213 (2022) 106835.
[10] P. Vannucci, General Anisotropic Elasticity, Anisotropic Elasticity, Springer, 2018, pp. 19–73.
[11] X. Huang, S. Greenhalgh, L. Han, X. Liu, Generalized effective Biot theory and seismic wave propagation in anisotropic, poroviscoelastic media, J. Geophys. Res., Solid Earth 127 (3) (2022) e2021JB023590.
[12] M. Shokrollahi, M. Eskandari-Ghadi, N. Khaji, A unified approach for stress wave propagation in transversely isotropic elastic and poroelastic layered media, Soil Dyn. Earthq. Eng. 157 (2022) 107152.
[13] M. Carroll, An effective stress law for anisotropic elastic deformation, J. Geophys. Res., Solid Earth 84 (B13) (1979) 7510–7512.
[14] R.M. Bowen, Compressible porous media models by use of the theory of mixtures, Int. J. Eng. Sci. 20 (6) (1982) 697–735.
[15] S.C. Cowin, S.B. Doty, Tissue Mechanics, Springer Science & Business Media, 2007.
[16] S.C. Cowin, Continuum Mechanics of Anisotropic Materials, Springer Science & Business Media, 2013.
[17] B. Markert, Y. Heider, W. Ehlers, Comparison of monolithic and splitting solution schemes for dynamic porous media problems, Int. J. Numer. Methods Eng. 82 (11) (2010) 1341–1383.
[18] J.N. Reddy, Introduction to the Finite Element Method, McGraw-Hill Education, 2019.
[19] T.J. Hughes, The Finite Element Method: Linear Static and Dynamic Finite Element Analysis, Courier Corporation, 2012.
[20] Z. Lotfian, M. Sivaselvan, Mixed finite element formulation for dynamics of porous media, Int. J. Numer. Methods Eng. 115 (2) (2018) 141–171.
[21] O.C. Zienkiewicz, R.L. Taylor, J.Z. Zhu, The Finite Element Method: Its Basis and Fundamentals, Elsevier, 2005.
[22] K.-J. Bathe, Finite Element Procedures for Solids and Structures Linear Analysis, Finite Element Procedures, Prentice-Hall, Upper Saddle River, NJ, 1982, pp. 148–214.
[23] H.A. van der Vorst, Bi-CGSTAB: a fast and smoothly converging variant of Bi-CG for the solution of non-symmetric linear systems, SIAM J. Sci. Stat. Comput. 13 (1992) 631–644.
[24] N. Castelletto, J.A. White, M. Ferronato, Scalable algorithms for three-field mixed finite element coupled poromechanics, J. Comput. Phys. 327 (2016) 894–918, https://doi.org/10.1016/j.jcp.2016.09.063.
[25] M. Ferronato, A. Franceschini, C. Janna, N. Castelletto, H.A. Tchelepi, A general preconditioning framework for coupled multiphysics problems with application to contact- and poro-mechanics, J. Comput. Phys. 398 (2019) 108887.
[26] A. Franceschini, L. Gazzola, M. Ferronato, A scalable preconditioning framework for stabilized contact mechanics with hydraulically active fractures, J. Comput. Phys. 463 (2022) 111276.

[27] N. De Marchi, V. Salomoni, N. Spiezia, Effects of finite strains in fully coupled 3D geomechanical simulations, Int. J. Geomech. 4 (2019) 04019008.
[28] N. De Marchi, W. Sun, V. Salomoni, Shear wave splitting and polarization in anisotropic fluid-infiltrating porous media: a numerical study, Materials 13 (21) (2020) 4988.
[29] S. Sharma, D.A. Siginer, Permeability measurement methods in porous media: a review, in: ASME International Mechanical Engineering Congress and Exposition, vol. 48715, 2008, pp. 179–200.
[30] R.W. Lewis, B.A. Schrefler, The Finite Element Method in the Static and Dynamic Deformation and Consolidation of Porous Media, John Wiley & Sons, 1998.
[31] Y. Saad, M.H. Schultz, GMRES: a generalized minimal residual algorithm for solving a nonsymmetric linear system, SIAM J. Sci. Stat. Comput. 7 (1986) 856–869.
[32] M. Benzi, Preconditioning techniques for large linear systems: a survey, J. Comput. Phys. 182 (2002) 418–477.
[33] M. Ferronato, Preconditioning for sparse linear systems at the dawn of the 21st century: history, current developments, and future perspectives, ISRN Appl. Math. 2012 (2012) 127647, https://doi.org/10.5402/2012/127647.
[34] A.J. Wathen, Preconditioning, Acta Numer. 24 (2015) 329–376, https://doi.org/10.1017/S0962492915000021.
[35] Q.M. Bui, L. Wang, D. Osei-Kuffuor, Algebraic multigrid preconditioners for two-phase flow in porous media with phase transitions, Adv. Water Resour. 114 (2018) 19–28.
[36] Q.M. Bui, D. Osei-Kuffuor, N. Castelletto, J.A. White, A scalable multigrid reduction framework for multiphase poromechanics of heterogeneous media, SIAM J. Sci. Comput. 42 (2) (2020) B379–B396.
[37] A. Franceschini, N. Castelletto, M. Ferronato, Approximate inverse-based block preconditioners in poroelasticity, Comput. Geosci. 25 (2021) 701–714.
[38] A. Brandt, J. Brannick, K. Kahl, I. Livshits, Bootstrap algebraic multigrid: status report, open problems, and outlook, Numer. Math., Theory Methods Appl. 8 (1) (2015) 112–135.
[39] P. D'Ambra, S. Filippone, P.S. Vassilevski, A software package for bootstrap AMG based on graph weighted matching, ACM Trans. Math. Softw. 44 (4) (2018) 1–25.
[40] V.A. Paludetto Magri, A. Franceschini, C. Janna, A novel algebraic multigrid approach based on adaptive smoothing and prolongation for ill-conditioned systems, SIAM J. Sci. Comput. 41 (1) (2019) A190–A219.
[41] A. Franceschini, M. Ferronato, M. Frigo, C. Janna, A reverse augmented constraint preconditioner for Lagrange multiplier methods in contact mechanics, Comput. Methods Appl. Mech. Eng. 392 (2022) 114632.
[42] R. de Boer, W. Ehlers, Z. Liu, One-dimensional transient wave propagation in fluid-saturated incompressible porous media, Arch. Appl. Mech. 1 (1993) 59–72, 63.